

# Bayesian nonparametric modeling of heterogeneous populations of networks

Francesco Barile<sup>1</sup>, Simón Lunagómez<sup>2</sup>, and Bernardo Nipoti<sup>1</sup>

<sup>1</sup>Department of Economics, Management and Statistics, University of Milano-Bicocca, Italy,

francesco.barile@unimib.it; bernardo.nipoti@unimib.it

<sup>2</sup>Instituto Tecnológico Autónomo de México, CDMX 01080, Mexico,

simon.lunagomez@itam.mx

## Abstract

The increasing availability of multiple network data has highlighted the need for statistical models for heterogeneous populations of networks. A convenient framework makes use of metrics to measure similarity between networks. In this context, we propose a novel Bayesian nonparametric model that identifies clusters of networks characterized by similar connectivity patterns. Our approach relies on a location-scale Dirichlet process mixture of centered Erdős–Rényi kernels, with components parametrized by a unique network representative, or mode, and a univariate measure of dispersion around the mode. We demonstrate that this model has full support in the Kullback–Leibler sense and is strongly consistent. An efficient Markov chain Monte Carlo scheme is proposed for posterior inference and clustering of multiple network data. The performance of the model is validated through extensive simulation studies, showing improvements over state-of-the-art methods. Additionally, we present an effective strategy to extend the application of the proposed model to datasets with a large number of nodes. We illustrate our approach with analysis of human brain network data.

**Keywords:** Centered Erdős–Rényi distribution, Consensus subgraph clustering, Dirichlet process, Multiple network data.

# 1 INTRODUCTION

In recent years, multiple network link relations on the same set of nodes have become prominent in many fields of application. For instance, in neuroscience, interconnections among brain regions are collected to characterize a population of individuals suffering from a neurological disorder (Nelson et al., 2017); in computer science, human mobility is studied by tracking individuals’ movements in relation to intelligent displays (Shaw et al., 2018). Multiple networks are also known as multiplex networks (Mucha et al., 2010) and can be intended either as multiple link relations among the nodes of the network (replicated networks) or as a single link relation observed over different conditions, such as one network evolving over time (longitudinal networks). The developments proposed in this work are motivated by the problem of modeling heterogeneous populations of networks, with a key application of our modeling approach being the clustering of multiple network data. For instance,

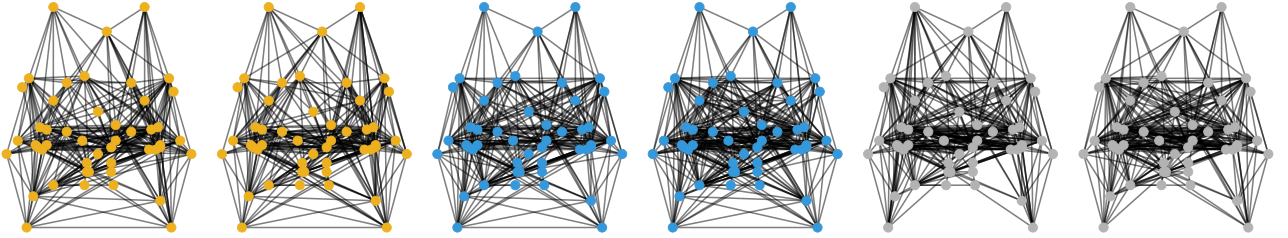


Figure 1: Top-down projection of a sample of six network observations extracted from the Human Brain Networks dataset (see Section 5 for details). The nodes of each network are colored according to the network cluster assignments, as inferred by the proposed method.

Figure 1 illustrates a sample of observations from the Human Brain Network dataset analyzed in Section 5, with networks colored based on the clusters inferred by our method. Notably, the approach successfully identifies clusters of similar networks, even when differences between networks are not visually evident.

Recent studies have extended modeling strategies originally designed for a single network observation to multiple network data. Three different, not necessarily disjoint, frameworks for multiple network data have been considered in the literature. The first one is defined through latent space models, with the occurrence of an edge between two nodes depending on the positions of the nodes in a latent space (Gollini and Murphy, 2016; Durante et al., 2017; Arroyo et al., 2021; Nielsen and Witten, 2018; Wang et al., 2021). A second one is based on the use of metrics to measure similarities among networks (Donnat and Holmes, 2018). Central to this framework is the notion of representative network, defined with respect to a probabilistic model induced by a suitable choice of metric on the space of networks, as a reference for a population (Ginestet et al., 2017; Lunagómez et al., 2021; Kolaczyk et al., 2017). Thirdly, measurement error models account for noise in network data by addressing the uncertainty associated with falsely observing edges or non-edges in a network (Young et al., 2022; Mantziou et al., 2024). Notably, Mukherjee et al. (2017) were the first to address the problem of clustering multiple

network data by defining a graphon mixture model. Le et al. (2018) develop a two-stage algorithm under the assumption that a network population can be summarized by a representative network with community structure, while accounting for a measurement error process that prevents an accurate observation of the representative network. Diquigiovanni and Scarpa (2019) propose a clustering approach that involves specifying an ad hoc measure of similarity between networks and implementing an agglomerative method to cluster the networks based on these similarities. Signorelli and Wit (2020) provide a model-based approach for clustering multiple network data with a predefined number of clusters, accounting for the presence of covariates. In line with Le et al. (2018), Mantziou et al. (2024) relax the unimodality assumption to accommodate heterogeneous network data by defining a mixture of measurement error models with a fixed and known number of components. A similar approach is proposed by Young et al. (2022), with the key difference being that the representative networks are not required to form communities in their structural topology.

We propose a structure-free modeling approach for multiple network data, where no constraints are imposed on the topology characterizing the data generative process. Our strategy accounts for the heterogeneity that may exist in a population of networks, without imposing rigid assumptions on the number of network subgroups driving the heterogeneity. Such flexibility is achieved by adopting a Bayesian nonparametric approach. The literature on nonparametric inferential methods for the distribution of network-valued random variables within a heterogeneous population of networks is very limited. A notable exception is Durante et al. (2017), who define a Bayesian nonparametric model for the joint distribution of edges using a mixture representation. To the best of our knowledge, no nonparametric methods have been devised for clustering multiple network data. We aim to address this gap by proposing a Bayesian nonparametric distance-based model that combines flexibility and tractability.

## 1.1 OUR CONTRIBUTION

We propose a location-scale Dirichlet process mixture of centered Erdős–Rényi kernels to model heterogeneous populations of networks. This kernel choice favors both analytical and computational tractability. The flexibility of the model is ensured by its full topological support, in the Kullback–Leibler sense, over the space of network distributions on a given set of nodes. Additionally, the model’s location-scale structure aids in the interpretability of posterior inference. We investigate the properties of the proposed model, present a strategy for posterior computation, demonstrate its effectiveness in various inferential tasks, and explore its applicability to large-dimensional data. The key contributions of this work can be summarized as follows:

- i) We prove that the proposed model possesses desirable theoretical features, including full support on the space of probability distributions on networks and posterior consistency.

- ii) We develop an efficient Gibbs sampler, relying on the availability of closed-form full conditional distributions for the model’s elements.
- iii) We show the model is effective for various inferential tasks, such as clustering networks, estimating probability mass functions, and making predictions.
- iv) Through simulations, we compare our method’s performance in tasks like clustering and probability mass function estimation, revealing notable improvements over existing approaches.
- v) We apply our method to a dataset from the HNU1 study (Zuo et al., 2014), which includes diffusion magnetic resonance imaging (dMRI) from multiple subjects, to demonstrate its practical application.
- vi) To handle clustering in populations of networks with many nodes, we introduce an approximate solution called consensus subgraph clustering.

The remainder of the article is organized as follows. In Section 2, we introduce a new model for multiple network data and study its main theoretical properties. Section 3 outlines a strategy for posterior computation and discusses its implementation. Section 4 presents extensive simulation studies comparing our model with existing methods. In Section 5, our method is applied to the analysis of a human brain network dataset. Section 6 introduces an approximate computational strategy for clustering large-dimensional datasets. Finally, Section 7 offers concluding remarks. Proofs and additional results are provided as Supplementary Material.

## 2 MODELING STRATEGY

### 2.1 PRELIMINARIES

A simple undirected labeled binary graph  $\mathcal{G} = (\mathcal{V}, \mathcal{E})$  consists of a set of labeled vertices  $\mathcal{V}$  and a set of edges  $\mathcal{E} \subseteq \{E \subseteq \mathcal{V} : |E| = 2\}$ , that is a subset of the set of pairs of distinct nodes. Given  $\mathcal{V}$ , we let  $\mathcal{G}_{\mathcal{V}}$  denote the set of all simple undirected labeled binary graphs with nodes  $\mathcal{V}$ , or graph space. While  $\mathcal{G}_{\mathcal{V}}$  is the main focus of this work, it is worth noting that both the modeling and computational strategies we introduce can be readily extended to directed graphs and graphs with self-relations. Given this, and for simplicity, we will henceforth refer to the elements of  $\mathcal{G}_{\mathcal{V}}$  simply as graphs or networks, with a slight abuse of terminology. We observe that, if  $N = |\mathcal{V}|$ , then  $|\mathcal{G}_{\mathcal{V}}| = 2^M$ , where  $M = \binom{N}{2}$  is the maximum number of edges that a graph with  $N$  nodes might feature. A graph  $\mathcal{G}$  can be represented by an  $N \times N$  adjacency matrix  $A_{\mathcal{G}}$  such that  $A_{\mathcal{G}[ij]} = 1$  if  $\{i, j\} \in \mathcal{E}$ , and  $A_{\mathcal{G}[ij]} = 0$  otherwise, where the subscript  $[ij]$  is used to indicate the element in position  $(i, j)$  of a matrix. The symmetry of the adjacency matrix  $A_{\mathcal{G}}$  follows from the fact that  $\mathcal{G}$  is assumed undirected. Finally, we point out that throughout this work we assume that all random variables are defined on the same probability space

$(\Omega, \mathcal{F}, \mathbb{P})$ .

We consider a dataset  $\mathcal{G}^{(1:n)} = \{\mathcal{G}_1, \dots, \mathcal{G}_n\}$  of multiple networks, that is a collection of multiple observations of networks with nodes  $\mathcal{V} = \{1, \dots, N\}$ . In other terms, for any  $l = 1, \dots, n$ , we have  $\mathcal{G}_l = (\mathcal{V}, \mathcal{E}_l)$ . This type of data is common, for instance, in medical imaging, with brain regions assigned to the nodes of a graph according to an atlas, and edges representing the connections recorded among regions. Modeling an observation  $\mathcal{G}_l$  is equivalent to modeling the  $M$ -dimensional vector  $\text{vech}(A_{\mathcal{G}_l})$  defined as the half-vectorization of  $A_{\mathcal{G}_l}$ , whose components coincide with the elements of the lower triangular half of  $A_{\mathcal{G}_l}$ . Given the finite dimensionality of  $\mathcal{G}_{\mathcal{V}}$ , a set  $\mathcal{G}^{(1:n)}$  of random graphs, each taking values in  $\mathcal{G}_{\mathcal{V}}$ , can be modeled using a categorical distribution. This can be achieved, for example, by employing latent class models (Goodman, 1974), which require the selection of an appropriate number of classes, or by resorting to the nonparametric tensor factorization model for multivariate unordered categorical data proposed by Dunson and Xing (2009). We pursue a different strategy by building upon the notion of a representative category to capture the presence of common underlying structures shared among different network configurations. The model we propose is based on the idea that distributions on the graph space are conveniently parameterized in terms of a mean, induced by a specified metric, and a measure of the distribution’s dispersion around this mean. The notion of Fréchet mean (Fréchet, 1948) is particularly useful as it generalizes the first moment to non-Euclidean settings, providing a tool to identify a measure of central tendency with respect to the specified metric. Assessing similarities among networks based on their global or local characteristics naturally allows us to evaluate variability in the space of graphs. Our modeling strategy thus requires the specification of a metric on the graph space to appropriately define network structural similarity (Donnat and Holmes, 2018) and to map non-Euclidean objects to standard spaces. The Hamming distance (Hamming, 1950), a special instance of the broader class of Graph-Edit distances, is arguably the simplest distance metric between two graphs. Defined as

$$d_{\text{H}}(\mathcal{G}_1, \mathcal{G}_2) = \sum_{i=1}^{N-1} \sum_{j=i+1}^N |A_{\mathcal{G}_1[ij]} - A_{\mathcal{G}_2[ij]}|,$$

the Hamming distance between two graphs measures the number of edge deletions and insertions necessary to transform one graph into another, thus capturing local changes, that is changes in the graph structure around each node. Working with the Hamming distance implies that additions and deletions are assumed to have similar importance. When compared to other distances, e.g. spectral distances, the Hamming distance offers the notable advantage of allowing the use of standard combinatorial tools. This proves useful for both specifying families of probability distributions for graphs and carrying out efficient posterior inference. An example of a probability distribution for unordered categorical data defined using the Hamming distance is provided in Argiento et al. (2024). In the

network literature, a flexible distribution for random graphs, defined using the Hamming distance, is the centered Erdős–Rényi (CER) (Lunagómez et al., 2021). The CER distribution arises as the product of independent but not identically distributed Bernoulli probability mass functions. The probability of an edge connecting two given nodes is either  $\alpha$  or  $1 - \alpha$ , depending on whether an edge is connecting the same pair of nodes of a central graph  $\mathcal{G}^m$ , which can be interpreted as graph mode. As a result, the scale of variation parameter  $\alpha$  drives the variability around  $\mathcal{G}^m$ . Formally, for any  $i < j$ ,  $\mathbb{P}(A_{\mathcal{G}[ij]} \neq A_{\mathcal{G}^m[ij]}) = 1 - \mathbb{P}(A_{\mathcal{G}[ij]} = A_{\mathcal{G}^m[ij]}) = \alpha$ . The joint distribution of the  $M$  components of  $\text{vech}(A_{\mathcal{G}})$  thus leads to an equivalent probability mass function for  $\mathcal{G}$ , that is

$$p_{\text{CER}}(\mathcal{G}; \mathcal{G}^m, \alpha) = \alpha^{d_{\text{H}}(\mathcal{G}, \mathcal{G}^m)} (1 - \alpha)^{M - d_{\text{H}}(\mathcal{G}, \mathcal{G}^m)}. \quad (1)$$

A random graph  $\mathcal{G}$ , taking values in  $\mathcal{G}_{\mathcal{V}}$  and with probability mass function (1), is said to have CER distribution with location parameter  $\mathcal{G}^m \in \mathcal{G}_{\mathcal{V}}$  and scale of variation parameter  $\alpha \in (0, 1/2)$ . We use the notation  $\mathcal{G} \sim \text{CER}(\mathcal{G}^m, \alpha)$ . Although (1) is well defined for any  $\alpha \in (0, 1)$ , restricting the set of values that  $\alpha$  can take to  $(0, 1/2)$  ensures that the resulting distribution is unimodal, with mode at  $\mathcal{G}^m$ . That is, if  $d_{\text{H}}(\mathcal{G}_1, \mathcal{G}^m) > d_{\text{H}}(\mathcal{G}_2, \mathcal{G}^m)$  then  $p_{\text{CER}}(\mathcal{G}_2; \mathcal{G}^m, \alpha) > p_{\text{CER}}(\mathcal{G}_1; \mathcal{G}^m, \alpha)$ , formalizing the idea that graphs closer to the graph mode are more likely. The CER distribution serves as the building block of the flexible Bayesian model that we introduce next.

## 2.2 A BAYESIAN NONPARAMETRIC MODEL

We introduce a Bayesian nonparametric model for networks, defined as a nonparametric location-scale mixture of CER kernels. The CER kernel function, denoted as  $\psi(\cdot; \cdot)$ , is defined on  $\mathcal{G}_{\mathcal{V}} \times \Theta$ , with  $\Theta = \mathcal{G}_{\mathcal{V}} \times (0, 1/2)$ . Specifically,  $\psi(\mathcal{G}; \vartheta = (\mathcal{G}^m, \alpha)) = p_{\text{CER}}(\mathcal{G}; \mathcal{G}^m, \alpha)$ , where  $p_{\text{CER}}$  is defined in (1). For simplicity, we define the nonparametric mixture model using the distribution of a Dirichlet process (DP). However, the posterior computation strategies presented in this work are easily adapted to more general mixing measures, as long as their predictive distribution is available in closed form. This is the case, for example, with the class of Gibbs-type priors (De Blasi et al., 2015), and, following the introduction of a suitable auxiliary random variable, with the class of normalized random measures with independent increments (Regazzini et al., 2003).

**Definition 1** (Location-scale DP mixture of CER kernels). *The location-scale DP mixture of CER kernels on  $\mathcal{G}_{\mathcal{V}}$  is the random probability mass function  $\tilde{f}$  defined as*

$$\tilde{f}(\cdot) = \int_{\Theta} \psi(\cdot; \vartheta) d\tilde{P}(\vartheta),$$

where  $\Theta = \mathcal{G}_{\mathcal{V}} \times (0, 1/2)$  and  $\tilde{P}$  is distributed as DP with base measure  $P_0$  on  $\Theta$ , and concentration parameter  $c > 0$ .

Following the introduction of the latent variables  $\vartheta^{(1:n)} = \{\vartheta_1, \dots, \vartheta_n\}$ , the same model can be expressed in hierarchical form as

$$\begin{aligned} \mathcal{G}_l &| \vartheta^{(1:n)} \stackrel{\text{ind}}{\sim} \psi(\mathcal{G}_l; \vartheta_l) & l = 1, \dots, n \\ \vartheta_l = (\mathcal{G}_l^m, \alpha_l) &| \tilde{P} \stackrel{\text{iid}}{\sim} \tilde{P} & l = 1, \dots, n \\ \tilde{P} &\sim \text{DP}(c, P_0). \end{aligned} \quad (2)$$

The DP mixture of CER kernels is completed by specifying the base measure  $P_0$ , which we define as the joint distribution of  $\vartheta = (\mathcal{G}^m, \alpha)$  for which

$$\begin{aligned} \alpha &\sim \text{TBeta}(1/2; a, b) \\ \mathcal{G}^m &| \alpha \sim \text{CER}(\mathcal{G}_0, \alpha), \end{aligned} \quad (3)$$

for some hyperparameters  $a, b > 0$ , and  $\mathcal{G}_0 \in \mathcal{G}_\mathcal{V}$ . For  $q \in (0, 1)$ ,  $\text{TBeta}(q; a, b)$  in (3) denotes the Truncated-Beta distribution on  $(0, q)$ , whose probability density function is given by

$$f_{\text{TBeta}}(\alpha; q, a, b) = \frac{\alpha^{a-1} (1 - \alpha)^{b-1}}{\mathcal{B}(q; a, b)},$$

where  $\mathcal{B}(q; a, b) = \int_0^q \alpha^{a-1} (1 - \alpha)^{b-1} d\alpha$  indicates the incomplete beta function. The proposed specification of  $P_0$  conveniently allows for the derivation of closed-form expressions for the conditional distributions of the latent variables  $\vartheta_l$  involved in the algorithm for posterior simulation described in Section 3. Finally, an additional level of hierarchy can be introduced in (2) by assuming a prior distribution for the model hyperparameters  $(a, b, c, \mathcal{G}_0)$ .

### 2.3 KULLBACK–LEIBLER PROPERTY AND POSTERIOR CONSISTENCY

We show that the location-scale DP mixture of CER kernels, introduced in Definition 1 and with base measure (3), has full support in the Kullback–Leibler sense. Specifically, for any  $\varepsilon > 0$ , the prior induced by  $\tilde{f}$  assigns positive probability to the Kullback–Leibler neighborhood  $\mathbb{B}_\varepsilon(p_*) = \{\omega \in \Omega : \text{KL}(p_*; \tilde{f}^{(\omega)}) \leq \varepsilon\}$  of any probability mass function  $p_* \in \mathcal{P}_{\mathcal{G}_\mathcal{V}}$ , where  $\text{KL}(p_*; \tilde{f}^{(\omega)})$  denotes the Kullback–Leibler divergence between the probability mass functions  $p_*$  and  $\tilde{f}^{(\omega)}$ ,  $\mathcal{P}_{\mathcal{G}_\mathcal{V}}$  denotes the space of all probability distributions on  $\mathcal{G}_\mathcal{V}$ , and  $\tilde{f}^{(\omega)}$  indicates a realization  $\tilde{f}$ . This property, also known as the Kullback–Leibler property, is appealing as it formalizes the idea that any distribution in  $\mathcal{P}_{\mathcal{G}_\mathcal{V}}$  can be approximated arbitrarily well by a set of realizations of  $\tilde{f}$  with positive prior probability. For Bayesian modeling, it is convenient to use priors with the Kullback–Leibler property, hence nonparametric, especially when there is no conclusive prior information about the parametric shape of the distribution generating the data (Walker et al., 2004). The Kullback–Leibler property is also

key in studying the large  $n$  behavior of the posterior distribution of  $\tilde{f}$ , given  $\mathcal{G}^{(1:n)}$ . Considering the finiteness of  $\mathcal{G}_{\mathcal{V}}$ , the Kullback–Leibler property implies that the posterior distribution of  $\tilde{f}$  is strongly consistent at any  $p_* \in \mathcal{P}_{\mathcal{G}_{\mathcal{V}}}$  (see, e.g., Example 6.21 in Ghosal and van der Vaart, 2017). These properties are formalized in Theorem 1 and Corollary 1.1. The proof of Theorem 1 is postponed to the Supplementary Material.

**Theorem 1.** *The prior  $\Pi$  induced by a location-scale DP mixture of CER kernels with base measure as in (3) has the Kullback–Leibler property. That is, for any  $p_* \in \mathcal{P}_{\mathcal{G}_{\mathcal{V}}}$  and any  $\varepsilon > 0$ ,  $\Pi(\mathbb{B}_{\varepsilon}(p_*)) > 0$ .*

Although Theorem 1 explicitly refers to the base measure in (3), its proof only relies on the fact that  $P_0$  has full support on  $\Theta$ . Therefore, the Kullback–Leibler property extends to any specification of the base measure with full support on  $\Theta$ .

**Corollary 1.1.** *The posterior distribution  $\Pi_n(\cdot \mid \mathcal{G}^{(1:n)})$  of a location-scale DP mixture of CER kernels with base measure as in (3), given  $\mathcal{G}^{(1:n)}$ , is strongly consistent at any  $p_* \in \mathcal{P}_{\mathcal{G}_{\mathcal{V}}}$ . That is, for any  $p_* \in \mathcal{P}_{\mathcal{G}_{\mathcal{V}}}$ ,  $\Pi_n(U_{p_*}^c \mid \mathcal{G}^{(1:n)}) \rightarrow 0$  almost surely, as  $n \rightarrow \infty$ , for any neighborhood  $U_{p_*}$  of  $p_*$ .*

It is worth noting that, while the literature on the asymptotic properties of models for networks typically focuses on the case where the number of nodes  $N \rightarrow \infty$  in a single network (see, e.g., Tang et al., 2013), Corollary 1.1 addresses the consistent estimation of the entire population distribution for a network-valued random variable, as the number of networks  $n \rightarrow \infty$ , with a fixed  $N$ . This theoretical result is supported by the simulation study presented in Section 4.2, which investigates how the posterior estimate concentrates around its true value as a function of sample size  $n$ .

### 3 POSTERIOR COMPUTATION

We adapt the marginal algorithm from Escobar and West (1995), originally introduced for location-scale DP mixtures of univariate Gaussian kernels, to mixtures of CER kernels, as specified in Definition 1 and (3). Posterior sampling is achieved through a Gibbs sampler, following the analytical marginalization of the DP  $\tilde{P}$ . Despite the inherently complex structure of  $\mathcal{G}_{\mathcal{V}}$ , the distributions involved in the algorithm are available in closed form, making posterior sampling conveniently efficient. The algorithm consists of sequential Gibbs updates of the individual parameters  $\vartheta_l = (\mathcal{G}_l^m, \alpha_l)$  from their full conditional distribution

$$\mathbb{P}\left(\vartheta_l \in \cdot \mid \vartheta_{(-l)}^{(1:n)}, \mathcal{G}^{(1:n)}\right) = \pi_{l0} P_l(\cdot) + \sum_{k=1}^{K_{(-l)}} \pi_{lk} \delta_{\vartheta_{k(-l)}^*}(\cdot), \quad (4)$$

where the subscript  $(-l)$  denotes quantities computed after removing  $\vartheta_l$  from  $\vartheta^{(1:n)}$ . Equation 4 represents the celebrated generalized Pólya urn scheme of Blackwell and MacQueen (1973), formalizing



the idea that  $\vartheta_l$  can either coincide with any of the distinct values in  $\vartheta_{(-l)}^{(1:n)}$ , that is  $\vartheta_{k(-l)}^*$ , with probability  $\pi_{lk}$ , for  $k = 1, \dots, K_{(-l)}$ , or take a new value with probability  $\pi_{l0}$ . The probabilities in (4) are given, up to a proportionality constant, by

$$\begin{aligned} \pi_{l0} &\propto c \sum_{r=0}^{M-d_l} w_{lr} \frac{\mathcal{B}(1/2; a_{lr}, b_{lr})}{\mathcal{B}(1/2; a, b)} \\ \pi_{lk} &\propto n_{k(-l)} \psi(\mathcal{G}_l; \vartheta_{k(-l)}^*) \quad k = 1, \dots, K_{(-l)}, \end{aligned} \quad (5)$$

where  $d_l = d_H(\mathcal{G}_0, \mathcal{G}_l)$ ,  $w_{lr} = 2^{d_l} \binom{M-d_l}{r}$ ,  $a_{lr} = a + 2r + d_l$  and  $b_{lr} = b + 2M - 2r - d_l$ . The distribution  $P_l$  of new values for  $\vartheta_l$  is, conditionally on  $\mathcal{G}_l$ , proportional to  $\psi(\mathcal{G}_l; \vartheta) dP_0(\vartheta)$ . Sampling from  $P_l$  translates into sampling from a mixture of Truncated-Beta distributions, and from  $M$  independent Bernoulli distributions. Specifically,  $\vartheta_l = (\mathcal{G}_l^m, \alpha_l) \mid \mathcal{G}_l \sim P_l$  can be expressed as

$$\alpha_l \mid \mathcal{G}_l \sim \sum_{r=0}^{M-d_l} \varphi_{lr} \text{TBeta}(1/2; a_{lr}, b_{lr}) \quad (6)$$

$$A_{\mathcal{G}_l^m[ij]} \mid \alpha_l, \mathcal{G}_l \stackrel{\text{ind}}{\sim} \text{Bern}(p_{lij}) \quad i < j, \quad (7)$$

where  $\varphi_{lr} \propto w_{lr} \mathcal{B}(1/2; a_{lr}, b_{lr})$  and

$$p_{lij} = \left( 1 + \left( \frac{\alpha_l}{1 - \alpha_l} \right)^{2(A_{\mathcal{G}_0[ij]} + A_{\mathcal{G}_l[ij]} - 1)} \right)^{-1}. \quad (8)$$

The probability  $p_{lij}$  of generating a graph mode with an edge connecting the nodes  $\{i, j\}$  thus depends on whether  $\mathcal{G}_0$  and  $\mathcal{G}_l$  display such an edge. See also Figure 8 in the Supplementary Material.

To improve the mixing of the algorithm, it is key to introduce a reshuffling step that independently updates the cluster labels, i.e., the values  $\vartheta_k^* = (\mathcal{G}_k^{m*}, \alpha_k^*)$  for  $k = 1, \dots, K$ , after each Gibbs sampling iteration (Bush and MacEachern, 1996). We let  $\mathcal{D}_k = \{l \in \{1, \dots, n\} : \vartheta_l = \vartheta_k^*\}$  be the index set of observations belonging to the  $k$ -th cluster, with  $|\mathcal{D}_k| = n_k$ , and define  $\mathcal{D}_k^\dagger = \mathcal{D}_k \cup \{0\}$ . For any index set  $\mathcal{D} \subseteq \{0, 1, \dots, n\}$ , we introduce the notation  $\mathcal{G}^{(\mathcal{D})} = \{\mathcal{G}_l : l \in \mathcal{D}\}$ , and we let  $n_{ij}^{(k)} = \sum_{l \in \mathcal{D}_k^\dagger} A_{\mathcal{G}_l[ij]}$  denote the number of graphs in  $\mathcal{G}^{(\mathcal{D}_k^\dagger)}$  that present an edge connecting the nodes  $\{i, j\}$ . Similarly to  $P_l$ , updating  $\vartheta_k^*$  from its full conditional distribution translates into sampling from a mixture of Truncated-Beta distributions, and from  $M$  independent Bernoulli distributions. Specifically, after introducing the quantities  $D_k^* = \sum_{i=1}^{N-1} \sum_{j=i+1}^N \max\{n_{ij}^{(k)}, n_k + 1 - n_{ij}^{(k)}\}$  and  $d_k^* = \sum_{i=1}^{N-1} \sum_{j=i+1}^N \min\{n_{ij}^{(k)}, n_k + 1 - n_{ij}^{(k)}\}$ ,

we can write

$$\alpha_k^* \mid \mathcal{G}^{(\mathcal{D}_k)} \sim \sum_{r=0}^{D_k^* - d_k^*} \varphi_{kr}^* \text{TBeta}(\alpha_k^*; 1/2, a_{kr}^*, b_{kr}^*) \quad (9)$$

$$A\mathcal{G}_k^{m^*}[ij] \mid \alpha_k^*, \mathcal{G}^{(\mathcal{D}_k)} \stackrel{\text{ind}}{\sim} \text{Bern}(p_{kij}^*), \quad i < j. \quad (10)$$

The Bernoulli parameters in (10) are defined as

$$p_{kij}^* = \left( 1 + \left( \frac{\alpha_k^*}{1 - \alpha_k^*} \right)^{2(n_{ij}^{(k)} - (n_k + 1)/2)} \right)^{-1}. \quad (11)$$

The probability  $p_{kij}^*$  to generate a graph mode with an edge connecting the nodes  $\{i, j\}$  is increasing in the number  $n_{ij}^{(k)}$  of graphs in  $\mathcal{D}_k^\dagger$  displaying such an edge. Moreover,  $p_{kij}^*$  is increasing in  $\alpha_k^*$  if  $n_{ij}^{(k)} < (n_k + 1)/2$  and decreasing if  $n_{ij}^{(k)} > (n_k + 1)/2$ . See also Figure 8 in the Supplementary Material.

The mixture weights in (9) are given, up to a proportionality constant, by

$$\varphi_{kr}^* \propto w_{kr}^* \mathcal{B}(1/2; a_{kr}^*, b_{kr}^*), \quad (12)$$

where  $a_{kr}^* = a + d_k^* + r$  and  $b_{kr}^* = b + (n_k + 1)M - d_k^* - r$ . In turn, the coefficients  $w_{kr}^*$  in (12) result from a generating function defined by a product of polynomials, embedding a subset-sum problem. Specifically, we have

$$w_{kr}^* = \begin{cases} \sum_{\mathcal{S}_{kr}} \prod_{h=0}^{n_k/2} \binom{M_{kh}}{s_h} & \text{if } n_k \text{ is even} \\ \sum_{\mathcal{R}_{kr}} 2^{m_k(\lfloor n_k/2 \rfloor + 1)} \prod_{h=0}^{\lfloor n_k/2 \rfloor} \binom{M_{kh}}{s_h} & \text{if } n_k \text{ is odd,} \end{cases} \quad (13)$$

where  $\lfloor x \rfloor$  denotes the integer part of  $x$ , the sums in (13) are taken over the sets

$$\mathcal{S}_{kr} = \left\{ (s_0, \dots, s_{n_k/2}) : s_h \in \{0, \dots, M_{kh}\} \forall h, \sum_{h=0}^{n_k/2} \gamma_{kh}(s_h) - d_k^* = r \right\},$$

$$\mathcal{R}_{kr} = \left\{ (s_0, \dots, s_{\lfloor n_k/2 \rfloor}) : s_h \in \{0, \dots, M_{kh}\} \forall h, \sum_{h=0}^{\lfloor n_k/2 \rfloor} \gamma_{kh}(s_h) + (\lfloor n_k/2 \rfloor + 1)m_{k(\lfloor n_k/2 \rfloor + 1)} - d_k^* = r \right\},$$

$m_{kh} = \#\{\{i, j\} \in \mathcal{V}^2 : n_{ij}^{(k)} = h\}$  indicates the number of pairs of nodes that are connected by an edge in exactly  $h$  graphs in  $\mathcal{G}^{(\mathcal{D}_k^\dagger)}$ ,  $M_{kh} = m_{kh} + m_{k(n_k+1-h)}$ , and  $\gamma_{kh}(s_h) = (n_k + 1 - 2h)s_h + hM_{kh}$ . We note that the conditions defining the sets  $\mathcal{S}_{kr}$  and  $\mathcal{R}_{kr}$ , for any  $k = 1, \dots, K$  and  $r = 0, \dots, D_k^* - d_k^*$ , represent linear Diophantine equations with the decision variables  $\{s_0, \dots, s_{\lfloor n_k/2 \rfloor}\}$  constrained by  $s_h \leq M_{kh}$ , for  $h = 1, \dots, \lfloor n_k/2 \rfloor$ . Moreover, as expected, when  $n_k = 1$ , that is  $\mathcal{D}_k = \{l\}$  for some

$l = 1, \dots, n$ , the distribution in (9) and (10) simplifies to the distribution  $P_l$ , in (6) and (7), for  $\vartheta_l$ , conditionally on  $\mathcal{G}_l$  and given that it takes a new value. The steps of the algorithm are summarized in Algorithm 1 in the Supplementary Material, which additionally presents a closed-form expression for the cluster-specific  $m$ -step-ahead posterior predictive distribution, obtained by building on the conditional distribution of  $\vartheta_k^*$ , as described in (9) and (10).

## 4 SIMULATION STUDY

We explore the behavior of the DP mixture of CER kernels through the analysis of synthetic data. The study has two objectives: (i) assessing the model’s ability to cluster multiple network data with a known partition structure, under data-generating processes characterized by varying levels of variability; and (ii) investigating the impact of sample size on the accuracy of posterior estimates. To facilitate graphical presentation, we focus on networks with  $N = 20$  nodes. Observations are sampled from a mixture of four CER components  $p_*(\cdot) = \sum_{k=1}^4 0.25 p_{\text{CER}}(\cdot; \mathcal{G}_{0k}^m, \alpha_{0k})$ , where well-defined component-specific network structures are defined through the modes  $\mathcal{G}_{0k}^m$ . Specifically, and in the same spirit as Durante et al. (2017), each component is centered around a network configuration, or centroid, with distinct structures: scale-free (Barabási and Albert, 1999) for  $\mathcal{G}_{01}^m$ , small-world (Watts and Strogatz, 1998) for  $\mathcal{G}_{02}^m$ , stochastic block model (Nowicki and Snijders, 2001) for  $\mathcal{G}_{03}^m$ , and Erdős–Rényi (Erdős and Rényi, 1960) for  $\mathcal{G}_{04}^m$ . This choice is designed to assess whether the proposed model can effectively cluster and estimate the distribution of a collection of multiple network data with heterogeneous underlying structures. The generated centroids are displayed in the first row of Figure 3. The specification of the parameters for the four models used to generate the centroids is summarized in Table 4 in the Supplementary Material. The study consists of two parts: in the first one, multiple network data are generated by considering various component-specific scales of variation while keeping the sample size fixed; in the second one, the sample size varies while the scale parameters of the data-generating models remain fixed. For both parts, we specify the parameters of the base measure (3) as follows. The centroid  $\mathcal{G}_0$  is set, by using an empirical Bayes approach, by looking at the sample Fréchet mean (see Lunagómez et al., 2021). Specifically,  $\mathcal{G}_0$  is the network that has an edge between the nodes  $\{i, j\}$  if and only if that edge is present in at least 50% of the networks in the dataset. The parameters  $a$  and  $b$  are both set equal to one, thus implying the prior model for the scale of variation parameter is centered at a uniform distribution on  $(0, 1/2)$ . Finally, the concentration parameter  $c$  is set equal to one.

For each scenario in the two simulation studies, 100 datasets are generated. Each dataset is analyzed by running 1,200 Gibbs iterations, with the first 200 discarded as burn-in. The results obtained with our model are compared with those obtained using the methods of Young et al. (2022) and Durante et al. (2017). Although not originally intended for this purpose, the latter can be naturally extended to

address clustering problems for multiple network data. This study suggests that, overall, our model is superior to state-of-the-art methods in two key aspects: effectively modeling a population of networks with heterogeneous characteristics and accurately clustering the elements of a network population.

#### 4.1 DATA-GENERATING MODELS WITH VARYING SCALES OF VARIATION

To assess the ability of a method to cluster multiple network data we compare the estimated partition to the true partition, which reflects the four-component mixture structure of the data-generating model. We resort to three metrics: clustering entropy, clustering purity, and the Rand index. A point estimate for the data partition is obtained from the posterior samples produced by Algorithm 1 in the Supplementary Material, by minimizing the posterior expected Variation of Information, as implemented in the `Salso` R package (Dahl et al., 2022). We investigate the robustness of our method in clustering multiple network data generated from models characterized by different levels of variability. To this end, we fix a sample size of  $n = 40$  and focus on four scenarios with increasing scale of variation parameters shared across all components. We also consider a more realistic scenario with different scales of variation for each of the four components of the data-generating model. The values of the component-specific scales of variation for these scenarios are reported in Table 1. The results of our

Level of variability	$\alpha_{01}$	$\alpha_{02}$	$\alpha_{03}$	$\alpha_{04}$
low	0.25	0.25	0.25	0.25
medium-low	0.30	0.30	0.30	0.30
medium	0.35	0.35	0.35	0.35
high	0.40	0.40	0.40	0.40
mixed	0.25	0.35	0.30	0.40

Table 1: Definition of five simulation scenarios through the specification of the scale of variation parameters  $\{\alpha_{01}, \dots, \alpha_{04}\}$  of the four CER components of  $p_*$ .

investigations are displayed in Figure 2. According to the considered metrics, our model outperforms the methods of Durante et al. (2017) and Young et al. (2022) across all scenarios, showing lower values for clustering entropy and higher values for clustering purity and the Rand index. As expected, scenarios characterized by higher levels of variability are more challenging for all methods. It is also instructive to explore the properties of the clusters identified by our method. Given the estimated partition and denoting by  $\hat{K}$  the corresponding number of clusters, we can produce cluster-specific point estimates for the centroids by looking at the Fréchet mean of the posterior distribution of  $\mathcal{G}_k^{m*}$ , for  $k = 1, \dots, \hat{K}$ . Specifically, we sample from the posterior distribution of  $\vartheta_k^*$  in (9) and (10), and consider the sample Fréchet mean of  $\mathcal{G}_k^{m*}$ . Alternatively, one can look at Equation 21 in the Supplementary Material. We henceforth refer to this as to the cluster-specific posterior Fréchet mean. For illustrative purposes, we focus on a randomly selected dataset generated from the mixed variability scenario. The second row of Figure 3 shows the posterior Fréchet mean for centroids of the four estimated clusters.

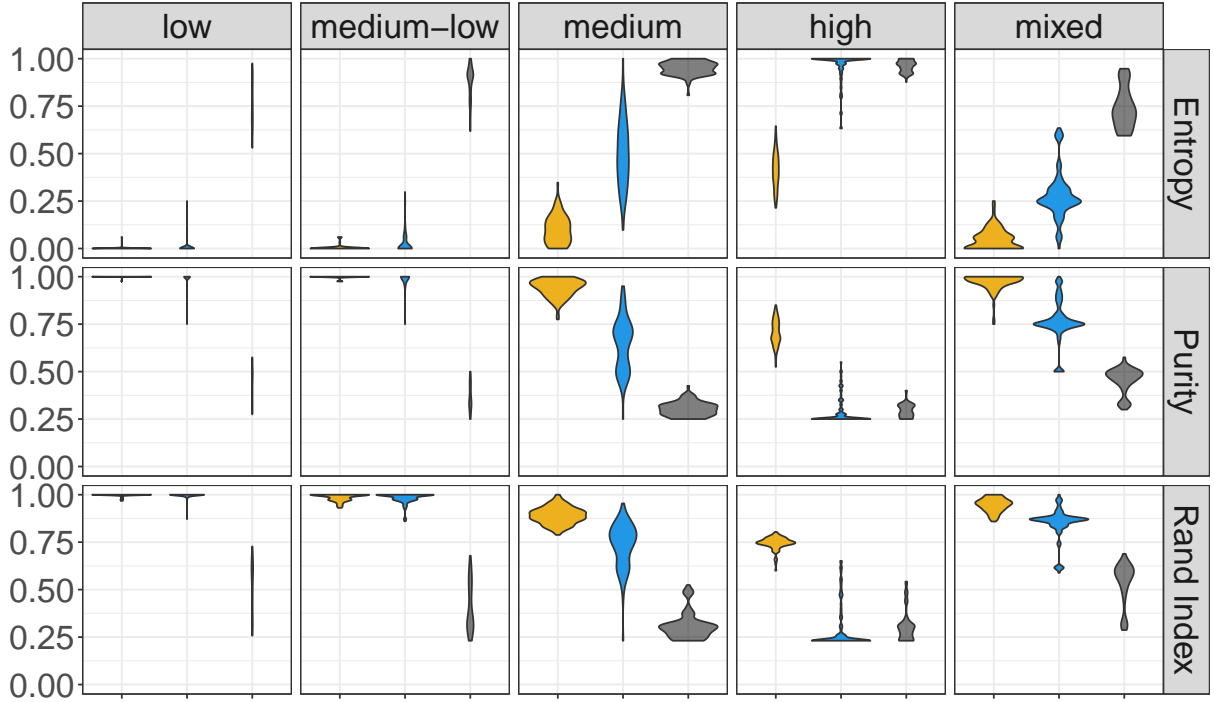


Figure 2: Entropy, purity, and the Rand index, for our method (yellow violins), and the methods of Durante et al. (2017) (blue violins) and Young et al. (2022) (gray violins). Columns refer to the scenarios of Table 1. Distributions are estimated based on the analysis of 100 datasets.

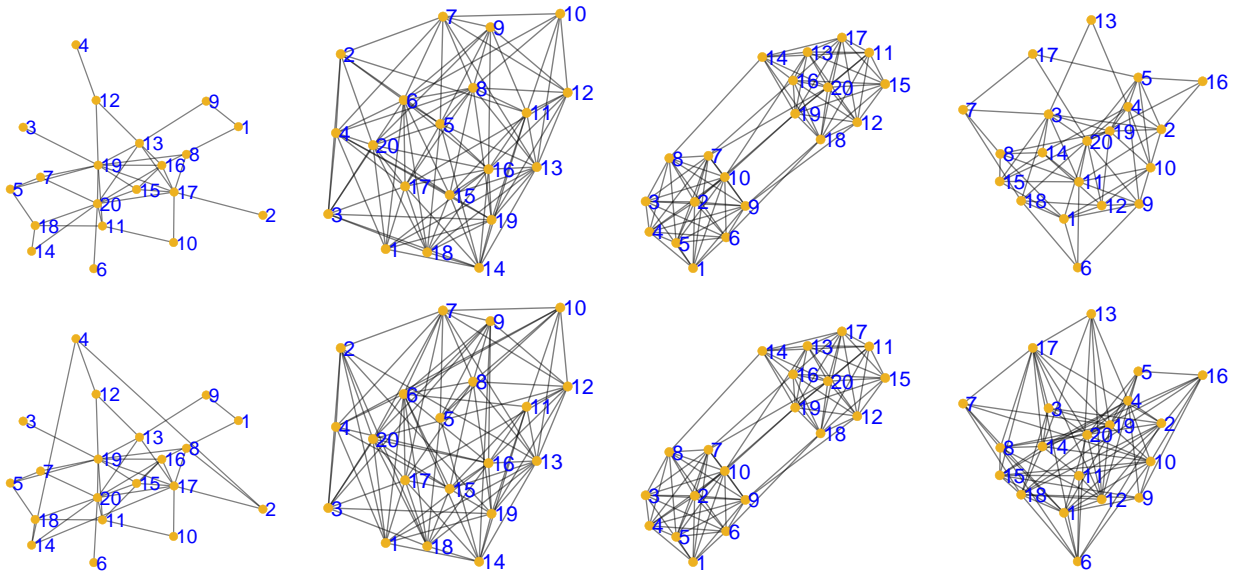


Figure 3: Top row: centroids with Scale-free ( $\mathcal{G}_{01}^m$ ), Small-world ( $\mathcal{G}_{02}^m$ ), Stochastic Block Model ( $\mathcal{G}_{03}^m$ ), and Erdős-Rényi ( $\mathcal{G}_{04}^m$ ) structures (from left to right). Bottom row: posterior Fréchet means for the four clusters estimated based on a dataset generated from the mixed level of variability scenario, with sample size  $n = 40$ .

The topological structures of these estimates align with those of the four-component data-generating mixture model, with the correspondence between true and estimated components identified based on the frequency of observations generated from a given component in the estimated clusters. Moreover, the point estimates of the cluster-specific scale parameters, that is  $\{0.262, 0.337, 0.295, 0.397\}$ , reflect

the heterogeneity in variability levels that characterize the data-generating model.

## 4.2 VARYING SAMPLE SIZE

We study the accuracy of the posterior mean  $\hat{f} = \mathbb{E}[\tilde{f} \mid \mathcal{G}^{(1:n)}]$  as an estimator of the true data-generating distribution  $p_*$ , with  $\hat{f}$  evaluated based on the posterior sample generated from Algorithm 1 in the Supplementary Material. Specifically, we investigate how this accuracy changes for different sample sizes  $n$ . This study aims to provide a finite-sample analogue to the strong consistency property of the DP mixture of CER kernels, as reported in Corollary 1.1, which states that for any  $\varepsilon > 0$ ,  $\mathbb{P}(d(p_*, \tilde{f}) > \varepsilon \mid \mathcal{G}^{(1:n)}) \rightarrow 0$ , almost surely, as  $n \rightarrow \infty$ , for a given metric  $d$  on  $\mathcal{P}_{\mathcal{G}_V}$ . Using the Kullback–Leibler divergence, we study the distribution of the distance between  $p_*$  and  $\hat{f}$  for finite samples of size  $n \in \{40, 80, 120, 200\}$ . The evaluation of  $\text{KL}(p_*; \hat{f})$  requires summation over the graph space  $\mathcal{G}_V$ , which is prohibitive even for moderate  $N$ . Thus, we propose an importance-sampling approximation of  $\text{KL}(p_*; \hat{f})$ :

$$\text{KL}(p_*; \hat{f}) = \sum_{\mathcal{G} \in \mathcal{G}_V} p_*(\mathcal{G}) \log \left( \frac{p_*(\mathcal{G})}{\hat{f}(\mathcal{G})} \right) = \mathbb{E}_{p_*} \left[ \log \left( \frac{p_*(\mathcal{G})}{\hat{f}(\mathcal{G})} \right) \right] \approx \frac{1}{L} \sum_{l=1}^L \log \left( \frac{p_*(\mathcal{G}_l)}{\hat{f}(\mathcal{G}_l)} \right),$$

with  $\mathcal{G}_l \stackrel{\text{iid}}{\sim} p_*$ , for  $l = 1, \dots, L$ . The results of our study are illustrated in Figure 4, which shows that

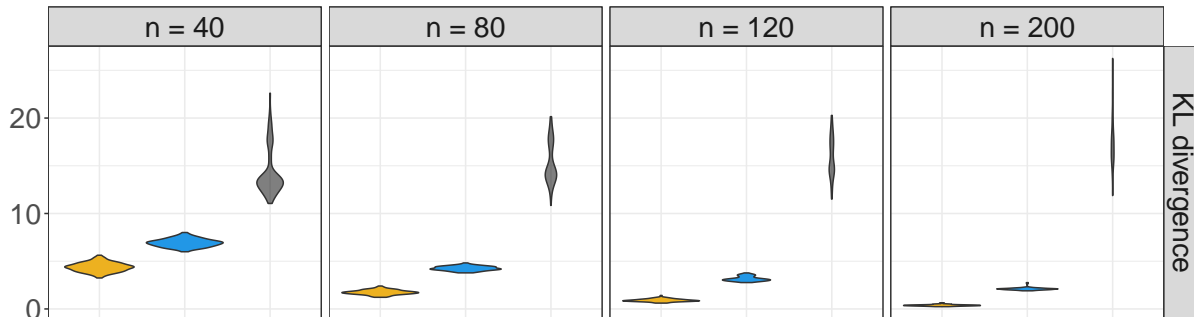


Figure 4: Importance-sampling approximate distributions of  $\text{KL}(p_*; \hat{f})$  for our method (yellow violins), and the methods of Durante et al. (2017) (blue violins) and Young et al. (2022) (gray violins). Distributions are estimated based on the analysis of 100 datasets.

the posterior estimate  $\hat{f}$  gets closer to  $p_*$  as the sample size increases. Our model appears to converge to  $p_*$  faster than the models proposed by Durante et al. (2017) and Young et al. (2022). Similar results, focusing on the  $L^1$  distance between  $p_*$  and  $\hat{f}$ , are presented in the Supplementary Material.

## 5 ANALYSIS OF HUMAN BRAIN NETWORKS DATA

We analyze a popular human brain dataset, publicly available at [https://networks.skewed.de/net/human\\_brains](https://networks.skewed.de/net/human_brains) (Peixoto, 2023), from the Consortium for Reliability and Reproducibility (CoRR) repos-

itory (Zuo et al., 2014). Connectivity patterns across different brain regions were measured for 30 healthy individuals at rest. Up to 10 measurements per individual were taken using diffusion magnetic resonance imaging (dMRI) over a month, totaling  $n = 266$  network observations. These measurements are represented as labeled networks with  $N = 48$  nodes corresponding to fixed brain regions of interest (ROI), defined by the ICBM DTI-81 atlas (Mori et al., 2008), and edges denoting connections among these regions. Two regions are considered connected if at least one white matter fiber links them. Importantly, fiber-tracking pipelines are subject to measurement errors. Figure 1 displays a sample of six observations from this dataset. The same dataset, though with different node granularity, has been discussed by Zuo et al. (2014), Arroyo et al. (2021), Lunagómez et al. (2021), and Mantziou et al. (2024). The latter three studies analyze the data from a modeling perspective. Arroyo et al. (2021) investigate their method’s ability to identify individual differences based on network communities. Lunagómez et al. (2021) assume unimodality in the network generation process and infer a representative network for the population. Mantziou et al. (2024) focus on detecting outlier networks. Our analysis aims to characterize differences in brain connectivity between subjects in the dataset. As in Section 4, we compare our model’s results with those obtained using the methods of Durante et al. (2017) and Young et al. (2022), where for the latter model we specified the number of mixture components equal to the number of subjects. Methods are first compared using posterior predictive checks, to assess their ability to recover the generative mechanism underlying the observed graphs for selected network summary measures. We simulate networks from the posterior predictive distribution, which for our model is given in (15) in the Supplementary Material, and compute network summary measures for these simulations. If the model lacks flexibility, we expect the observed data’s network measures to fall in the tails of their corresponding posterior predictive distributions. Figure 5 shows that the DP mixture of CER kernels and the method of Durante et al. (2017) are more flexible than the method of Young et al. (2022) in capturing the variability underlying functionals of the posterior predictive distribution. Some of the considered network summary measures, e.g. transitivity, indicate a slightly better fit of the model of Durante et al. (2017).

We next investigate whether brain scans of the same subject tend to be assigned to the same cluster and thus can be considered similar, a relevant question for researchers in neuroscience. We do this by comparing the estimated partition of the sample of network data, with the partition implied by the presence of 30 subjects in the study. Clustering metrics reported in Table 2 clearly indicate that our model detects similarities among the brain scans of the same individual, further validating its effectiveness in consistently clustering networks. Our model outperforms both the methods of Durante et al. (2017) and Young et al. (2022) in terms of clustering accuracy. The optimal partition identified by our model consists of 50 clusters, thus exceeding the number of subjects in the study. Only two clusters contain networks from different individuals, while for four subjects, the networks correspond-

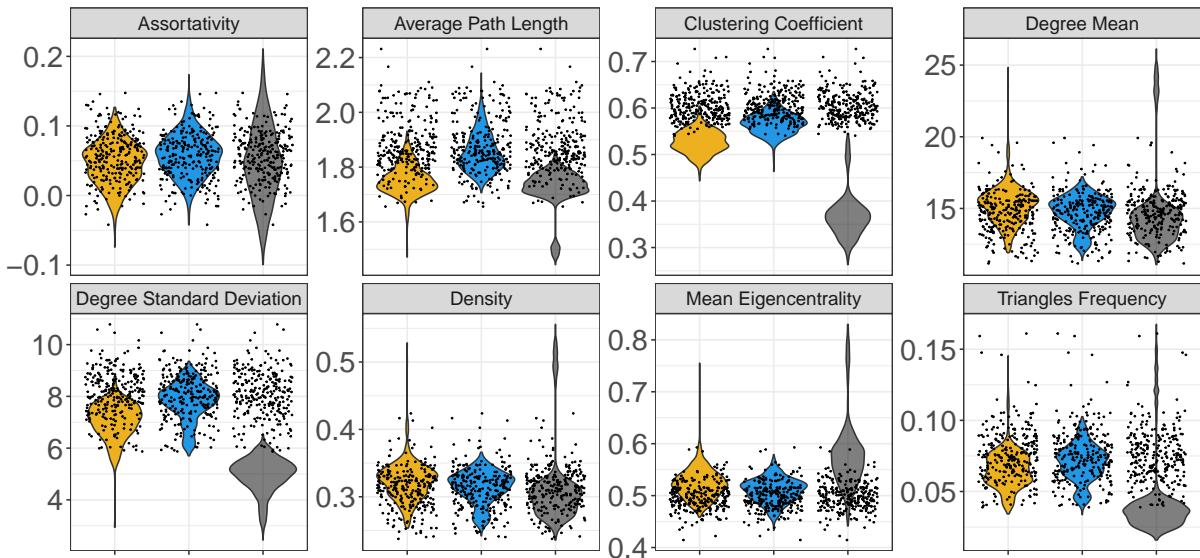


Figure 5: Posterior predictive checks. Posterior predictive distribution for selected network summary measures, for our method (yellow violins), and the methods of Durante et al. (2017) (blue violins) and Young et al. (2022) (gray violins). Jittered dots represent the network summary measures computed for the observed brain network data.

Model	$\hat{K}$	Entropy	Purity	Rand Index
DPM-CER	50	0.0065	0.9925	0.9902
Durante et al.	17	0.223	0.5677	0.9597
Young et al.	7	0.7833	0.1579	0.7493

Table 2: Clustering results of the Human Brain data set in terms of number of inferred clusters and clustering metrics with respect to the natural partition implied by individuals. Findings are compared with the models of Durante et al. (2017) and Young et al. (2022).

ing to the same subject are distributed across multiple clusters. These results hold potential biological significance, offering valuable insights for further investigation.

We conclude our analysis by evaluating whether the clusters identified by our model display features with neuroscientific interpretability. A similar question is addressed by Mantziou et al. (2024), who identify a subgroup of individuals with brain connectivity patterns distinct from the majority, based on network summary measures of interest to neuroscientists. We focus on average path length and clustering coefficient, two metrics of neuroscientific significance as human brains are known to typically exhibit a small-world structure, characterized by short average path lengths and high clustering coefficients (Bassett and Bullmore, 2006).

The left panel of Figure 6 shows the average shortest path length and clustering coefficient for the brain networks, for the three largest clusters of the estimated partition. The three clusters have size 10 and coincide with the scans of three subjects in the dataset. There is a clear distinction between the brain scans in each cluster with respect to these two network properties. This confirms our model’s ability to identify differences among data characterized by topological structures indicative of small-world



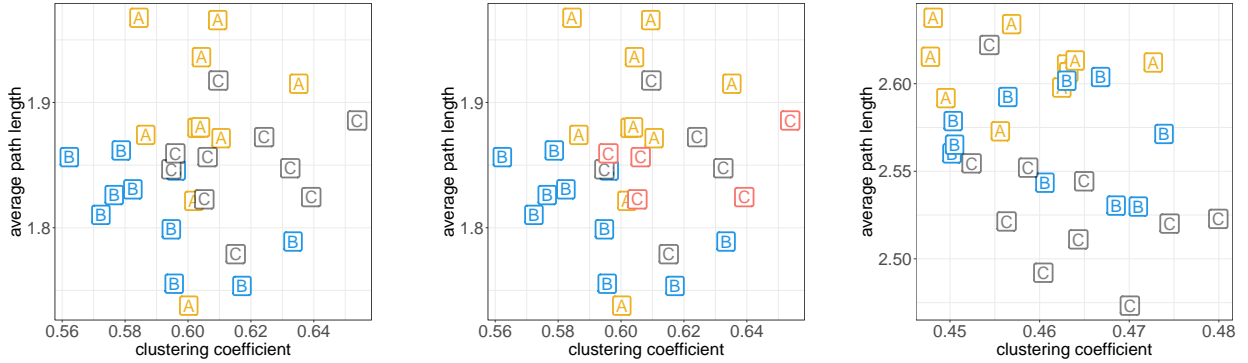


Figure 6: Scatter plots for the small-world properties of brain networks for three subjects in the dataset. Colors indicate the cluster membership, letters refer to the subject ID in the dataset, namely 0025443 (A), 0025445 (B) and 0025446 (C). Left panel:  $N = 48$ , partition estimated via DP mixture of CER kernels. Central and right panels:  $N = 48$  and  $N = 200$  respectively, partition estimated via consensus subgraph clustering (see Section 6).

behavior.

## 6 CONSENSUS SUBGRAPH CLUSTERING FOR LARGE $N$

Probabilistic models for network data often become computationally infeasible when the number of nodes is large (Jordan, 2004). This issue is exacerbated when dealing with multiple network data. Our method, for instance, becomes computationally intensive as  $N$  grows, requiring numerical evaluations that significantly slow down Algorithm 1 in the Supplementary Material. In addition, the computational burden increases with  $n$ . To address the challenge of clustering elements within a population of networks when the number of nodes is large, we propose a heuristic approach inspired by consensus clustering techniques (Strehl and Ghosh, 2002), which we call *consensus subgraph clustering*. Similar to variational methods, our approach breaks down some dependencies between nodes and measures similarity among networks based on their local characteristics. This is achieved by running our model-based clustering method in parallel on subgraph observations. Subgraphs are created by partitioning the  $N$  nodes into blocks of at most  $N_{\text{sub}}$  nodes. This step is akin to assuming a block structure at the vertex level, with block memberships assigned based on available information, e.g. spatial, on the nodes. Each Gibbs sampler produces a sample of partitions of the multiple network data from the posterior distribution of the model, conditional on the subgraphs obtained by restricting the original data to specific node blocks. The subgraph-specific posterior samples are then pooled into a unique sample, from which we identify a representative partition by minimizing the posterior expected Variation of Information. We illustrate this strategy through the analysis of a version of the human brain network data analyzed in Section 5, with  $N = 200$  and thus characterized by finer node granularity.

## 6.1 BRAIN NETWORK DATA WITH FINER GRANULARITY

Constructed from the same  $n = 266$  dMRI scans of 30 healthy individuals already analyzed in Section 5, the dataset we consider is based on the CC200 human brain atlas (Craddock et al., 2012), which includes  $N = 200$  ROIs, and is available in the same repository. Compared to the 48 ROIs considered in Section 5, this version presents a substantially higher dimensionality, posing a greater computational challenge. We implement the described consensus subgraph clustering approach and start by investigating the effect of  $N_{\text{sub}}$  on the estimated data partition. We consider subgraphs defined on mutually exclusive vertex sets with cardinality at most equal to  $N_{\text{sub}} \in \{5, 10, 15, 20, 25, 30, 35, 40, 50\}$ , which leads, respectively, to  $m_{\text{sub}} \in \{40, 20, 14, 10, 8, 7, 6, 5, 4\}$  distinct datasets of multiple network data of dimension at most  $N_{\text{sub}}$ . Nodes are divided into  $m_{\text{sub}}$  blocks based on the physical distance between ROIs, using a balanced clustering technique (Grötschel and Wakabayashi, 1989), as implemented in the `anticlust` R package (Papenberg and Klau, 2021). This approach reduces dependencies between the most distant nodes, as illustrated in Figure 14 in the Supplementary Material. For each subgraph we thus have  $n = 266$  observations, corresponding to the restriction of the original network data to a subset of nodes. Conditionally on each sample of subgraphs, we run Algorithm 1 for 1,200 iterations, of which the first 200 are discarded as burn-in.

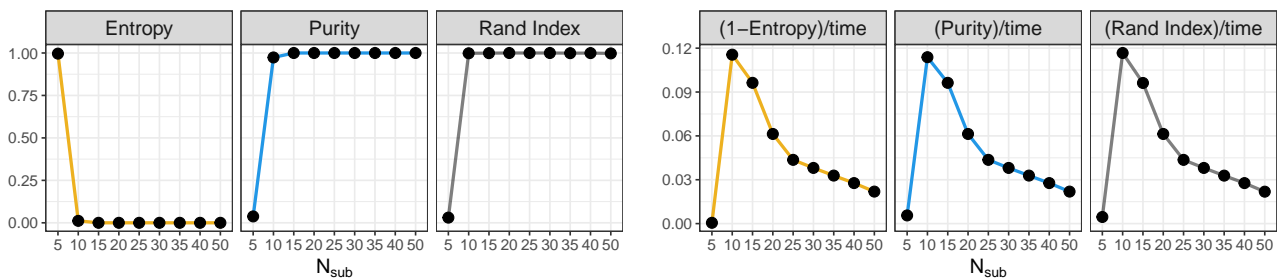


Figure 7: Clustering metrics comparing the partition estimated based on the consensus subgraph approach, with the one implied by the 30 individuals in the study, for the Human Brain dataset based on 200 ROIs, for  $N_{\text{sub}}$  ranging in  $\{5, 10, \dots, 50\}$ .

As in Section 5, we assess the accuracy of the estimated partition by comparing it to the one implied by the presence of 30 subjects in the study. The three panels on the left of Figure 7 show the values of three summary metrics for the considered values of  $N_{\text{sub}}$ . The consensus subgraph clustering approach struggles to correctly discriminate individual brain scans based on local characteristics when subgraphs with 5 nodes are used. However, when the analysis is conducted using subgraphs with at least 10 nodes, the method successfully captures the heterogeneity inherent in the brain networks of the 30 individuals. This experiment suggests that, as long as the subgraphs are not too small, examining local differences in connectivity patterns of subregions of the brain may be sufficient to detect overall similarities and differences across brain network data. Selecting an optimal  $N_{\text{sub}}$  involves balancing accuracy and

$N (N_{\text{sub}})$	$\hat{K}$	Entropy	Purity	Rand Index
48 (15)	34	0.1407	0.7932	0.9793
200 (10)	30	0.0115	0.9737	0.9983

Table 3: Human brain dataset. Estimated number of clusters and clustering metrics with respect to the partition implied by the presence of 30 individuals in the study.

computational time. The three right panels of Figure 7 display the ratios of the three clustering summary metrics already considered, relative to the computational time. To improve interpretability, we used  $1 - \text{Entropy}$  instead of rescaling the Entropy directly. For each value of  $N_{\text{sub}}$ , the computational time is defined as the maximum time taken to analyze any of the  $m_{\text{sub}}$  datasets. Since these datasets can be analyzed in parallel, this definition of computational time represents the total time needed by a machine with unlimited cores. It is apparent that, for  $N_{\text{sub}} \geq 15$ , the extra computational cost is not rewarded in terms of accuracy. Therefore, it seems reasonable to select a value for  $N_{\text{sub}}$  by looking at where the time-rescaled clustering metrics are maximized, which for this dataset is  $N_{\text{sub}} = 10$ . For comparison, we conducted a similar study on the effectiveness of the consensus subgraph clustering approach using the Human Brain dataset based on 48 ROIs, dataset for which we can compare the approximate posterior distribution with the exact one, as studied in Section 5. The results, displayed in Figure 15 in the Supplementary Material, lead to selecting  $N_{\text{sub}} = 15$ .

Table 3 compares the results of the consensus subgraph clustering method applied to the human brain datasets with 48 and 200 ROIs, where  $N_{\text{sub}}$  was set equal to 15 and 10 respectively, and the summary metrics computed by comparing the estimated partition with that one implied by the presence of 30 subjects in the study. It can be appreciated that the summary metrics indicate a better performance of our method when analyzing the dataset with finer granularity. The results referring to the case  $N = 48$  appear slightly worse than those obtained by applying our model on the entire graph observations, presented in Table 2. While it is clear that exploring only local properties of the graphs might reduce the ability to detect global properties of the graphs, these results indicate that the consensus subgraph clustering approach might be considered a valid alternative to cluster multiple network data when the number of nodes is large. Finally and for simplicity of illustration, we focus on the cluster allocation of the 30 observations referring to the three subjects assigned to the three largest clusters in the analysis run in Section 5. The central and right panels of Figure 6 display the cluster allocation of these 30 observations, obtained by resorting to the consensus subgraph clustering approach to analyze the human brain datasets with  $N = 48$  and  $N = 200$ , respectively, and highlight the topological properties of the identified clusters. Cluster allocation for the two cases resembles the results obtained in Section 5 when analyzing the complete dataset with  $N = 48$  ROIs, as shown in the left panel of Figure 6. The only notable difference is that the consensus subgraph clustering applied to the dataset with 48 ROIs separates the scans of the subject labeled ‘‘C’’ into two distinct clusters.

## 7 DISCUSSION

We introduced a novel Bayesian nonparametric approach to model heterogeneous populations of networks. The model’s location-scale structure favors interpretability while offering appealing theoretical properties, such as full support in the space of labeled graphs and posterior consistency. A key feature of our approach is that the proposed algorithm samples from distributions that are available in closed form. These distributions are derived using standard combinatorial arguments, which is made possible by the use of the Hamming distance to detect structural similarities among networks. As demonstrated in Section 4 and the brain network data analysis in Section 5, our model exhibits greater flexibility and achieves substantial performance gains over alternative methods from the literature. The model’s implementation results in a per-iteration computational cost that is quadratic in  $N$ . As a result, implementing our model can become computationally intensive when large values for  $N$  are considered. To address this challenge, we proposed a heuristic approach, named consensus subgraph clustering, designed to handle large-dimensional problems efficiently. Our analysis of human brain data with finer node granularity, as presented in Section 6, demonstrates that this method performs well with larger networks and shows promise for scaling to the analysis of massive networks. Interestingly, while the method was presented by utilizing the spatial locations of the ROIs represented by network nodes, promising results were also obtained when nodes were partitioned randomly, disregarding the available spatial information. This is illustrated in the Supplementary Material. Moreover, alternative strategies for node partitioning could be explored, to implement the preliminary step of the consensus subgraph clustering approach. For example, resorting to the concept of signal-subgraphs introduced by Vogelstein et al. (2012) could offer a promising direction.

The modeling strategy we presented offers multiple avenues for extension, opening up new research directions. An intriguing one involves exploring alternatives to the Hamming distance. Although the Hamming distance stands out for its tractability, it falls short in capturing the broader structural changes within a graph. For instance, in brain networks, spectral distances can better assess global changes in connectivity. A potential extension of our work in this direction could involve employing the *diffusion* distance, which is based on the graph Laplacian and treats objects functionally, focusing on changes that impact the global structure (Lunagómez et al., 2021). However, this approach may lack closed-form expressions, necessitating alternative computational strategies. Another interesting direction involves using our model as a foundational block for modeling related populations of networks in a partially exchangeable setting. This could be achieved by inducing dependence at the level of population-specific mixing measures, such as through the Dependent Dirichlet process (MacEachern, 2000), thereby facilitating the sharing of information across models (see Quintana et al., 2022, for a recent review).

## REFERENCES

- Argiento, R., E. Filippi-Mazzola, and L. Paci (2024). Model-based clustering of categorical data based on the hamming distance. *arXiv:2212.04746*.
- Arroyo, J., A. Athreya, J. Cape, G. Chen, C. Priebe, and J. Vogelstein (2021, 03). Inference for multiple heterogeneous networks with a common invariant subspace. *Journal of Machine Learning Research* 22, 1–49.
- Barabási, A.-L. and R. Albert (1999). Emergence of scaling in random networks. *Science* 286(5439), 509–512.
- Bassett, D. S. and E. Bullmore (2006). Small-world brain networks. *The Neuroscientist* 12(6), 512–523.
- Blackwell, D. and J. B. MacQueen (1973). Ferguson Distributions Via Polya Urn Schemes. *The Annals of Statistics* 1(2), 353 – 355.
- Bush, C. A. and S. N. MacEachern (1996). A semiparametric bayesian model for randomised block designs. *Biometrika* 83(2), 275–285.
- Craddock, R. C., G. James, P. E. Holtzheimer III, X. P. Hu, and H. S. Mayberg (2012). A whole brain fmri atlas generated via spatially constrained spectral clustering. *Human Brain Mapping* 33(8), 1914–1928.
- Dahl, D. B., D. J. Johnson, and P. Müller (2022). Search algorithms and loss functions for bayesian clustering. *Journal of Computational and Graphical Statistics* 31(4), 1189–1201.
- De Blasi, P., S. Favaro, A. Lijoi, R. H. Mena, I. Prunster, and M. Ruggiero (2015, feb). Are gibbs-type priors the most natural generalization of the dirichlet process? *IEEE Transactions on Pattern Analysis & Machine Intelligence* 37(02), 212–229.
- Diquigiovanni, J. and B. Scarpa (2019). Analysis of association football playing styles: An innovative method to cluster networks. *Statistical Modelling* 19(1), 28–54.
- Donnat, C. and S. Holmes (2018). Tracking network dynamics: A survey using graph distances. *The Annals of Applied Statistics* 12(2), 971–1012.
- Dunson, D. B. and C. Xing (2009). Nonparametric bayes modeling of multivariate categorical data. *Journal of the American Statistical Association* 104(487), 1042–1051.
- Durante, D., D. B. Dunson, and J. T. Vogelstein (2017). Nonparametric bayes modeling of populations of networks. *Journal of the American Statistical Association*.

- Erdős, P. and A. Rényi (1960). On the evolution of random graphs. *Publ. Math. Inst. Hungary. Acad. Sci.* 5, 17–61.
- Escobar, M. D. and M. West (1995). Bayesian density estimation and inference using mixtures. *Journal of the American Statistical Association* 90(430), 577–588.
- Fréchet, M. (1948). Les éléments aléatoires de nature quelconque dans un espace distancié. *Annales de l'institut Henri Poincaré* 10(4), 215–310.
- Ghosal, S. and A. van der Vaart (2017). *Fundamentals of Nonparametric Bayesian Inference*. Cambridge Series in Statistical and Probabilistic Mathematics. Cambridge University Press.
- Ginestet, C. E., J. Li, P. Balachandran, S. Rosenberg, and E. D. Kolaczyk (2017). Hypothesis testing for network data in functional neuroimaging. *The Annals of Applied Statistics* 11(2), 725 – 750.
- Gollini, I. and T. B. Murphy (2016). Joint modeling of multiple network views. *Journal of Computational and Graphical Statistics* 25(1), 246–265.
- Goodman, L. A. (1974). Exploratory latent structure analysis using both identifiable and unidentifiable models. *Biometrika* 61(2), 215–231.
- Grötschel, M. and Y. Wakabayashi (1989, aug). A cutting plane algorithm for a clustering problem. *Mathematical Programming* 45(1), 59–96.
- Hamming, R. W. (1950). Error detecting and error correcting codes. *The Bell System Technical Journal* 29(2), 147–160.
- Jordan, M. I. (2004). Graphical Models. *Statistical Science* 19(1), 140–155.
- Kolaczyk, E. D., L. Lin, S. J. Rosenberg, J. Xu, and J. Walters (2017). Averages of unlabeled networks: Geometric characterization and asymptotic behavior. *The Annals of Statistics*.
- Le, C. M., K. Levin, and E. Levina (2018). Estimating a network from multiple noisy realizations. *Electronic Journal of Statistics* 12(2), 4697 – 4740.
- Lunagómez, S., S. C. Olhede, and P. J. Wolfe (2021). Modeling network populations via graph distances. *Journal of the American Statistical Association* 116(536), 2023–2040.
- MacEachern, S. N. (2000). Dependent dirichlet processes. *Unpublished manuscript, Department of Statistics, The Ohio State University* 5.
- Mantziou, A., S. Lunagómez, and R. Mitra (2024). Bayesian model-based clustering for populations of network data. *The Annals of Applied Statistics* 18(1), 266–302.

- Mori, S., K. Oishi, H. Jiang, L. Jiang, X. Li, K. Akhter, K. Hua, A. V. Faria, A. Mahmood, R. Woods, A. W. Toga, G. B. Pike, P. R. Neto, A. Evans, J. Zhang, H. Huang, M. I. Miller, P. van Zijl, and J. Mazziotta (2008). Stereotaxic white matter atlas based on diffusion tensor imaging in an icbm template. *NeuroImage* 40(2), 570–582.
- Mucha, P. J., T. Richardson, K. Macon, M. A. Porter, and J.-P. Onnela (2010). Community structure in time-dependent, multiscale, and multiplex networks. *Science* 328(5980), 876–878.
- Mukherjee, S. S., P. Sarkar, and L. Lin (2017). On clustering network-valued data. *Advances in Neural Information Processing Systems* 30.
- Nelson, B., D. Bassett, J. Camchong, E. Bullmore, and K. Lim (2017, 05). Comparison of large-scale human brain functional and anatomical networks in schizophrenia. *NeuroImage: Clinical* 15.
- Nielsen, A. M. and D. Witten (2018). The multiple random dot product graph model. *arXiv:1811.12172*.
- Nowicki, K. and T. A. B. Snijders (2001). Estimation and prediction for stochastic blockstructures. *Journal of the American Statistical Association* 96(455), 1077–1087.
- Papenberg, M. and G. W. Klau (2021). Using anticlustering to partition data sets into equivalent parts. *Psychological Methods* 26(2), 161–174.
- Peixoto, T. P. (2023, April). The netzschleuder network catalogue and repository.
- Quintana, F. A., P. Müller, A. Jara, and S. N. MacEachern (2022). The dependent dirichlet process and related models. *Statistical Science* 37(1), 24–41.
- Regazzini, E., A. Lijoi, and I. Prünster (2003). Distributional results for means of normalized random measures with independent increments. *The Annals of Statistics* 31(2), 560–585.
- Shaw, P., M. Mikusz, P. Nurmi, and N. Davies (2018). Tacita: A privacy preserving public display personalisation service. In *Proceedings of the 2018 ACM International Joint Conference and 2018 International Symposium on Pervasive and Ubiquitous Computing and Wearable Computers*, pp. 448–451.
- Signorelli, M. and E. C. Wit (2020). Model-based clustering for populations of networks. *Statistical Modelling* 20(1), 9–29.
- Strehl, A. and J. Ghosh (2002, 01). Cluster ensembles - a knowledge reuse framework for combining multiple partitions. *Journal of Machine Learning Research* 3, 583–617.

- Tang, M., D. L. Sussman, and C. E. Priebe (2013). Universally consistent vertex classification for latent positions graphs. *The Annals of Statistics* 41(3), 1406 – 1430.
- Vogelstein, J. T., W. G. Roncal, R. J. Vogelstein, and C. E. Priebe (2012). Graph classification using signal-subgraphs: Applications in statistical connectomics. *IEEE Transactions on Pattern Analysis and Machine Intelligence* 35(7), 1539–1551.
- Walker, S., P. Damien, and P. Lenk (2004). On priors with a kullback–leibler property. *Journal of the American Statistical Association* 99(466), 404–408.
- Wang, S., J. Arroyo, J. T. Vogelstein, and C. E. Priebe (2021). Joint embedding of graphs. *IEEE Transactions on Pattern Analysis and Machine Intelligence* 43(4), 1324–1336.
- Watts, D. J. and S. H. Strogatz (1998). Collective dynamics of ‘small-world’ networks. *Nature* 393(6684), 440–442.
- Young, J.-G., A. Kirkley, and M. E. J. Newman (2022). Clustering of heterogeneous populations of networks. *Physical Review E* 105, 014312.
- Zuo, X.-N., J. Anderson, P. Bellec, R. Birn, B. Biswal, J. Blautzik, J. Breitner, R. Buckner, V. Calhoun, F. Castellanos, A. Chen, B. Chen, J. Chen, X. Chen, S. Colcombe, W. Courtney, C. Craddock, A. Di Martino, H. Dong, and M. Milham (2014). An open science resource for establishing reliability and reproducibility in functional connectomics. *Scientific Data* 1, 1–13.



## Supplementary Material for “Bayesian nonparametric modeling of heterogeneous populations of networks”

The Supplementary Material is organized as follows. In Section A we provide the proof of the results in Section 2.3. Section B provides additional details on the posterior computational strategy presented in Section 3. In particular, the steps of the proposed algorithm for posterior computations are summarized in Algorithm 1, and additional computational aspects to improve the efficiency of the algorithm are discussed. Section C presents a closed-form expression for the cluster-specific one-step-ahead posterior predictive distribution. Specifically, given an estimated partition of the sample of multiple network data, we analyze the conditional distribution of a new graph, assuming it belongs to a specific cluster. This result is generalized to make a joint prediction on  $m$  graphs, assuming that they all belong to a specific cluster of the estimated partition. In addition, the cluster-specific posterior distribution of  $\mathcal{G}_k^{m*}$  is also provided in closed-form. Finally, Section D and Section E present further information on the simulation studies of Section 4 and the illustration of Section 6.

### A PROOF OF THEOREM 1

*Proof.* As mentioned in Section 2.1,  $\mathcal{G}_V$  consists of  $|\mathcal{G}_V| = 2^M$  possible network configurations, with  $M = \binom{N}{2}$ . We can then name the elements of  $\mathcal{G}_V$  as  $\mathcal{G}_V = \{\mathcal{H}_1, \mathcal{H}_2, \dots, \mathcal{H}_{2^M}\}$ . We observe that any probability mass function  $p_* \in \mathcal{P}_{\mathcal{G}_V}$  is characterized by a set of  $2^M$  weights  $p_{0l} = p_*(\mathcal{H}_l)$ , with  $l = 1, \dots, 2^M$ , as

$$p_*(\cdot) = \sum_{l=1}^{2^M} p_{0l} \delta_{\mathcal{H}_l}(\cdot).$$

By exploiting the stick-breaking representation of the DP (Sethuraman, 1994), we can rewrite  $\tilde{f}$  as

$$\tilde{f}(\cdot) = \sum_{j=1}^{\infty} \tilde{p}_j \psi(\cdot; \tilde{\vartheta}_j),$$

where  $\tilde{\vartheta}_j = (\tilde{\mathcal{G}}_j^m, \tilde{\alpha}_j) \stackrel{\text{iid}}{\sim} P_0$  and the  $\tilde{p}_j$ 's are positive stick-breaking weights, such that  $\sum_{j=1}^{\infty} \tilde{p}_j = 1$  almost surely. We observe that, as done for  $p_*$ , also  $\tilde{f}$  can be written as a finite sum, that is

$$\tilde{f}(\cdot) = \sum_{l=1}^{2^M} \tilde{q}_l \delta_{\mathcal{H}_l}(\cdot).$$

For any  $\omega \in \Omega$ , we henceforth use the superscript  $(\omega)$  to denote a realization of a random variable, e.g.  $\tilde{f}^{(\omega)}$ .

For any  $\varepsilon > 0$ , we consider  $(\alpha_\star, \eta_\star)$  such that

- a1)  $0 < \alpha_\star < 1 - \exp\{-\varepsilon/M\}$ ;
- a2)  $0 < \eta_\star < 1 - \exp\{-\varepsilon\}/(1 - \alpha_\star)^M$ .

Given  $p_\star \in \mathcal{P}_{\mathcal{G}_N}$ , we let  $\tilde{f}^{(\omega)}$  be such that, for any  $l = 1, \dots, 2^M$ ,

- b1)  $\tilde{\mathcal{G}}_l^{m(\omega)} = \mathcal{H}_l$ ;
- b2)  $\tilde{p}_l^{(\omega)} \in [p_{0l}(1 - \eta_\star), p_{0l}]$ ;
- b3)  $\tilde{\alpha}_l^{(\omega)} \in (0, \alpha_\star]$ .

We observe that condition **a1** guarantees that the set of solutions  $\{\eta_\star : \mathbf{a2} \text{ holds}\}$  is not empty. We next show that if  $\tilde{f}^{(\omega)}$  satisfies **b1**, **b2**, and **b3**, then  $\text{KL}(p_\star; \tilde{f}^{(\omega)}) \leq \varepsilon$ . We first observe that, for any  $l = 1, \dots, 2^M$ ,

$$\tilde{q}_l^{(\omega)} \stackrel{\mathbf{b1}}{\geq} \tilde{p}_l^{(\omega)} (1 - \tilde{\alpha}_l^{(\omega)})^M. \quad (14)$$

Then, it follows that

$$\begin{aligned} \text{KL}(p_\star; \tilde{f}^{(\omega)}) &= \sum_{l=1}^{2^M} p_{0l} \log \left( \frac{p_{0l}}{\tilde{q}_l^{(\omega)}} \right) \\ &\stackrel{(14)}{\leq} \sum_{l=1}^{2^M} p_{0l} \log \left( \frac{p_{0l}}{\tilde{p}_l^{(\omega)} (1 - \tilde{\alpha}_l^{(\omega)})^M} \right) \\ &\stackrel{\mathbf{b2}}{\leq} \sum_{l=1}^{2^M} p_{0l} \log \left( \frac{1}{(1 - \eta_\star)(1 - \tilde{\alpha}_l^{(\omega)})^M} \right) \\ &\stackrel{\mathbf{b3}}{\leq} \sum_{l=1}^{2^M} p_{0l} \log \left( \frac{1}{(1 - \eta_\star)(1 - \alpha_\star)^M} \right) \\ &= \log \left( \frac{1}{(1 - \eta_\star)(1 - \alpha_\star)^M} \right) \stackrel{\mathbf{a2}}{\leq} \varepsilon. \end{aligned}$$

The proof is completed by showing that, for any  $\varepsilon > 0$ ,  $\Pi$  assigns positive probability to  $\mathbb{B}_\varepsilon(p_\star)$ . We observe that

$$\begin{aligned} \mathbb{B}_\varepsilon(p_\star) &\supseteq \{\omega \in \Omega : \mathbf{b1}, \mathbf{b2}, \mathbf{b3} \text{ hold for } (\alpha_\star, \eta_\star) \text{ satisfying } \mathbf{a1}, \mathbf{a2}\} \\ &= \{\omega \in \Omega : \mathbf{b1}, \mathbf{b3} \text{ hold for } (\alpha_\star, \eta_\star) \text{ satisfying } \mathbf{a1}, \mathbf{a2}\} \\ &\quad \cap \{\omega \in \Omega : \mathbf{b2} \text{ holds for } (\alpha_\star, \eta_\star) \text{ satisfying } \mathbf{a1}, \mathbf{a2}\} \\ &= A_1 \cap A_2. \end{aligned}$$

Given the independence of weights  $(\tilde{p}_j)_{j \geq 1}$  and atoms  $(\tilde{v}_j)_{j \geq 1}$  in the definition of  $\tilde{f}$ , the events  $A_1$  and  $A_2$  are disjoint and thus  $\Pi(A_1 \cap A_2) = \Pi(A_1)\Pi(A_2)$ . To prove that  $\Pi(\mathbb{B}_\varepsilon(p_*)) > 0$ , it then suffices to check that both  $\Pi(A_1)$  and  $\Pi(A_2)$  are positive.  $\Pi(A_1) > 0$  follows from the fact that  $P_0$  has full support on  $\Theta$ . Moreover,  $\Pi(A_2) > 0$  as, for any  $j = 1, 2, \dots$ , the distribution of  $\tilde{p}_j$  for the DP has full support on  $[0, 1 - \sum_{i=1}^{j-1} \tilde{p}_i]$ .  $\square$

## B FURTHER DETAILS ON POSTERIOR COMPUTATIONS

### B.1 ALGORITHM

Algorithm 1 summarizes the steps of the algorithm introduced in Section 3.

---

**Algorithm 1** Gibbs sampler for DP mixture of CER kernels

---

**Input:**  $\mathcal{G}^{(1:n)}$ ,  $a$ ,  $b$ ,  $c$ ,  $\mathcal{G}_0$

**Output:**  $\vartheta_{(1:T)} = (\vartheta_{(1)}, \dots, \vartheta_{(T)}) = (\vartheta_1^{(1:n)}, \dots, \vartheta_T^{(1:n)}) \triangleright (n \times (M+1) \times T)$ -dimensional array

```

1: Initialize:  $\vartheta_{(0)} \leftarrow \vartheta_0^{(1:n)} = (\vartheta_1^{(0)}, \vartheta_2^{(0)}, \dots, \vartheta_n^{(0)})$ 
2: for  $t \leftarrow 1$  to  $T$  do
3:   for  $l \leftarrow 1$  to  $n$  do  $\triangleright$  generalized Pólya urn scheme
4:      $\vartheta_{t(-l)}^{(1:n)} \leftarrow (\vartheta_1^{(t)}, \dots, \vartheta_{l-1}^{(t)}, \vartheta_{l+1}^{(t-1)}, \dots, \vartheta_n^{(t-1)})$ 
5:      $\vartheta_{t(-l)}^{*(1:K_{t(-l)})} \leftarrow (\vartheta_{1(-l)}^{*(t)}, \dots, \vartheta_{K_{t(-l)}(-l)}^{*(t)})$ 
6:      $\tilde{\pi}_{l0} \leftarrow c \sum_{r=0}^{M-d_l} w_{lr} \frac{\mathcal{B}(1/2; a_{lr}, b_{lr})}{\mathcal{B}(1/2; a, b)}$ 
7:     for  $k \leftarrow 1$  to  $K_{t(-l)}$  do
8:        $\tilde{\pi}_{lk}^{(t)} \leftarrow n_{k(-l)}^{(t)} \psi(\mathcal{G}_l; \vartheta_{k(-l)}^{*(t)})$ 
9:     end for
10:     $\tilde{\pi}_l^{(t)} \leftarrow (\tilde{\pi}_{l0}, \tilde{\pi}_{l1}^{(t)}, \dots, \tilde{\pi}_{lK_{t(-l)}}^{(t)})$   $\triangleright$  unnormalized probabilities
11:     $\pi_l^{(t)} = (\pi_{l0}, \pi_{l1}^{(t)}, \dots, \pi_{lK_{t(-l)}}^{(t)}) \leftarrow \left( \frac{\tilde{\pi}_{l0}}{\langle \mathbf{1}, \tilde{\pi}_l^{(t)} \rangle}, \frac{\tilde{\pi}_{l1}^{(t)}}{\langle \mathbf{1}, \tilde{\pi}_l^{(t)} \rangle}, \dots, \frac{\tilde{\pi}_{lK_{t(-l)}}^{(t)}}{\langle \mathbf{1}, \tilde{\pi}_l^{(t)} \rangle} \right)$ 
12:     $\zeta_l^{(t)} \sim \text{Cat}(K_{t(-l)} + 1, \pi_l^{(t)}) - 1$ 
13:    if  $\zeta_l^{(t)} = 0$  then
14:       $\vartheta_l^{(t)} \sim P_l$ 
15:    else
16:       $\vartheta_l^{(t)} \leftarrow \vartheta_{\zeta_l^{(t)}(-l)}^{*(t)}$ 
17:    end if
18:  end for
19:   $\vartheta_t^{(1:n)} \leftarrow (\vartheta_1^{(t)}, \dots, \vartheta_n^{(t)})$ 
20:   $\vartheta_t^{*(1:K_t)} \leftarrow (\vartheta_1^{*(t)}, \dots, \vartheta_{K_t}^{*(t)})$   $\triangleright$  reshuffling step
21:  for  $k \leftarrow 1$  to  $K_t$  do
22:     $\vartheta_k^{*(t)} \sim p(\vartheta_k^* | \mathcal{G}^{(\mathcal{D}_k^{(t)})})$ 
23:  end for
24:   $\vartheta_t^{*(1:K_t)} \leftarrow (\vartheta_1^{*(t)}, \dots, \vartheta_{K_t}^{*(t)})$ 
25:   $\vartheta_t^{(1:n)} \leftarrow (\vartheta_1^{(t)}, \dots, \vartheta_n^{(t)})$ 
26:   $\vartheta_{(t)} \leftarrow \vartheta_t^{(1:n)}$ 
27: end for
28:  $\vartheta_{(1:T)} \leftarrow (\vartheta_{(1)}, \dots, \vartheta_{(T)})$ 
29: return  $\vartheta_{(1:T)}$ 

```

---

## B.2 ADDITIONAL COMPUTATIONAL DETAILS

The Gibbs sampling in Algorithm 1 allows us to sample from the posterior distribution of  $\vartheta^{(1:n)}$  conditionally on  $\mathcal{G}^{(1:n)}$ . Some simple observations can help improving its efficiency.

The first one is that in the first step of the sampler, generating a new  $\vartheta_l$ , for all  $l$ , has a computational complexity of the order of  $\mathcal{O}(nM)$ , which can become an issue for larger network dimensions and/or population sizes. However, the unnormalized probability of sampling a new value for  $\vartheta_l$ , given in (5) and denoted by  $\tilde{\pi}_{l0}$  in step 6 of Algorithm 1, and the distribution  $P_l$  of new values for  $\vartheta_l$ , conditionally on  $\mathcal{G}_l$ , defined in (6)-(7), are iteration-invariant, if the hyperparameter  $\mathcal{G}_0$  is kept fixed. These quantities can thus be computed once before running the Gibbs sampler.

Secondly, in the reshuffling step, the update of  $\vartheta_k^* = (\mathcal{G}_k^{m*}, \alpha_k^*)$  has a computational complexity of the order of  $\mathcal{O}(KM)$ , with  $K$  being the number of clusters at a given iteration. Although, this step of the sampler may present a lower computational complexity, as  $K \leq n$ , calculations are more involved because the solution of a set of linear Diophantine equations is required for each  $k$  to compute the coefficients  $w_{kr}^*$  defined in (13) and appearing in the mixture weights given in (12). The number of equations to solve for each  $k$  depends on  $N$  and  $n_k$  through  $D_k^* - d_k^*$ . The complexity of each equation directly depends on  $n_k$ . Some considerations are worth noting. Let  $e_{kh} = n_k + 1 - 2h$  for  $h = 0, \dots, \lfloor n_k/2 \rfloor$ , and let  $g_k$  denote the common greatest divisor of the vector  $e_k = (e_{k0}, e_{k1}, \dots, e_{k\lfloor n_k/2 \rfloor})$ , namely  $g_k = \text{cgd}(e_k)$ . The linear Diophantine equation defining the set  $\mathcal{S}_{kr}(\mathcal{R}_{kr})$  has no solution when  $r + d_k^* - \sum_{h=0}^{\lfloor n_k/2 \rfloor} hM_{kh} \left( r + d_k^* - (\lfloor n_k/2 \rfloor + 1)m_{k(\lfloor n_k/2 \rfloor + 1)} - \sum_{h=0}^{\lfloor n_k/2 \rfloor} hM_{kh} \right)$  is not multiple of  $g_k$ . In this case,  $w_{kr}^* = 0$ . Moreover, the coefficient  $w_{kr}^*$  is symmetric with respect to the index  $r$ , that is  $w_{kr}^* = w_{k\bar{r}}^*$ , with  $\bar{r} = D_k^* - d_k^* - r$ . With these arguments, the overall computational time needed to define the set  $\mathcal{S}_{kr}(\mathcal{R}_{kr})$  can be more than halved. From a practical perspective, this can be solved with the algorithm based on a generating function of Halberstam (1967), used by Voinov and Nikulin (1997) and implemented in the `nilde` R package (Arnvist et al., 2022), by imposing  $\sum_{h=0}^{\lfloor n_k/2 \rfloor} s_h \leq M_k$ , where  $M_k = \sum_{h=0}^{\lfloor n_k/2 \rfloor} M_{kh}$  and retaining only the feasible solutions, that is those satisfying  $s_h \in \{0, \dots, M_{kh}\} \forall h$ . Yet, defining the set  $\mathcal{S}_{kr}(\mathcal{R}_{kr})$  at each iteration for any  $k = 1, \dots, K$  and  $r = 0, \dots, D_k^* - d_k^*$  substantially increases the computational time required in the reshuffling step. An alternative and cheaper strategy consists in replacing the conditional distribution of  $\alpha_k^*$  given  $\mathcal{G}^{(\mathcal{D}_k)}$  in (9) by its full conditional. That is  $\alpha_k^* \mid \mathcal{G}_k^{m*}, \mathcal{G}^{(\mathcal{D}_k)} \sim \text{TBeta}(1/2; a_k^*, b_k^*)$  where  $a_k^* = a + \sum_{l \in \mathcal{D}_k^\dagger} d_H(\mathcal{G}_l, \mathcal{G}_k^{m*})$  and  $b_k^* = b + (n_k + 1)M - \sum_{l \in \mathcal{D}_k^\dagger} d_H(\mathcal{G}_l, \mathcal{G}_k^{m*})$ . Sampling  $\alpha_k^*$  from its full conditional finds justification in that, along the chain, it targets the distribution in (9). Yet in this step, noting that the Bernoulli random variables given in (10) are identically distributed for all pairs of nodes  $\{i, j\}$  sharing the same value of  $n_{ij}^{(k)} = h$ , only  $m_{kh} \leq M$  Bernoulli parameters  $p_{kij}^*$  defined in (11) must be computed.

## C POSTERIOR PREDICTION

### C.1 POSTERIOR EDGE PROBABILITIES

We focus on the edge probabilities  $p_{lij}$ , defined in (8), and  $p_{kij}^*$  defined in (11). The left panel of

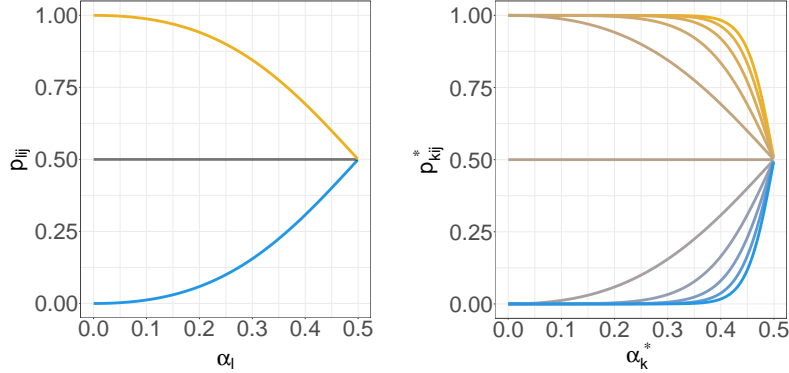


Figure 8: Left panel: probability  $p_{lij}$  in (8), with  $A_{\mathcal{G}_0[ij]} + A_{\mathcal{G}_l[ij]} \in \{0, 1, 2\}$  (blue for 0, gray for 1, and yellow for 2) and for  $\alpha_l$  ranging in  $(0, 1/2)$ . Right panel: probability  $p_{kij}^*$  in (11), with  $n_{ij}^{(k)} \in \{0, 1, \dots, n_k + 1\}$ ,  $n_k + 1 = 10$ , (blue for low, yellow for high) and for  $\alpha_k^*$  ranging in  $(0, 1/2)$ .

Figure 8 illustrates the dependence of  $p_{lij}$  on  $A_{\mathcal{G}_0[ij]} + A_{\mathcal{G}_l[ij]}$  and  $\alpha_l$ . The right panel of Figure 8 illustrates how the probability  $p_{kij}^*$  to generate a graph mode with an edge connecting the nodes  $\{i, j\}$  changes with the number  $n_{ij}^{(k)}$  of graphs in  $\mathcal{D}_k^\dagger$  displaying such an edge, for  $\alpha_k^*$  varying in  $(0, 1/2)$ . It is apparent that the larger the  $n_{ij}^{(k)}$ , the higher the probability that  $A_{\mathcal{G}_k^{m^*}[ij]} = 1$ , with this difference being more substantial for small values of  $\alpha_k^*$ .

### C.2 CLUSTER-SPECIFIC POSTERIOR PREDICTIVE DISTRIBUTION

The posterior predictive distribution implied by the statistical model defined in (1) is

$$p(\mathcal{G}^* | \mathcal{G}^{(1:n)}) = \int_{\Theta} \psi(\mathcal{G}^*; \vartheta) dp(\vartheta | \mathcal{G}^{(1:n)}) \quad (15)$$

where  $p(\vartheta | \mathcal{G}^{(1:n)})$  denotes the posterior distribution of  $\vartheta = (\mathcal{G}^m, \alpha)$ . Although the above integral is not analytically available, it is straightforward to simulate networks from the posterior predictive distribution exploiting MCMC samples for  $\vartheta$  along with the predictive distribution structure of the underlying DP. On the other hand, conditionally on an estimated partition of the observed graphs, cluster-specific one-step-ahead posterior predictive distribution implied by our model is available in closed-form. Predicting a graph  $\mathcal{G}^*$  from the posterior predictive distribution specific to the cluster of observations with indices in  $\mathcal{D}_k$  translates into sampling  $M$  independent Bernoulli distributions. Specifically,

$$A_{\mathcal{G}^*[ij]} | \mathcal{G}^{(\mathcal{D}_k)} \stackrel{\text{ind}}{\sim} \text{Bern}(\tilde{p}_{kij}), \quad i < j. \quad (16)$$

After introducing the quantities  $T_{kij}^* = \sum_{\{u,v\} \neq \{i,j\}} \max\{n_{uv}^{(k)}, n_k + 1 - n_{uv}^{(k)}\}$  and  $t_{kij}^* = \sum_{\{u,v\} \neq \{i,j\}} \min\{n_{uv}^{(k)}, n_k + 1 - n_{uv}^{(k)}\}$  where  $n_{uv}^{(k)} = \sum_{l \in \mathcal{D}_k^*} A_{\mathcal{G}_l[uv]}$ , the Bernoulli parameters in (16) are given by:

$$\tilde{p}_{kij} = \mathbb{E} \left[ A_{\mathcal{G}^*[ij]} \mid \mathcal{G}^{(\mathcal{D}_k)} \right] = \frac{1}{p(\mathcal{G}^{(\mathcal{D}_k)})} \sum_{r=0}^{T_{kij}^* - t_{kij}^*} \tilde{w}_{kr} \frac{\left[ \mathcal{B}(1/2; \tilde{a}_{kij}^{(r)}, \tilde{b}_{kij}^{(r)}) + \mathcal{B}(1/2; \tilde{c}_{kij}^{(r)}, \tilde{d}_{kij}^{(r)}) \right]}{\mathcal{B}(1/2; a, b)}, \quad (17)$$

where  $\tilde{a}_{kij}^{(r)} = a + n_{ij}^{(k)} + t_{kij}^* + r + 1$ ,  $\tilde{b}_{kij}^{(r)} = b + (n_k + 1)M - (n_{ij}^{(k)} + t_{kij}^* + r)$ ,  $\tilde{c}_{kij}^{(r)} = a + n_k + 1 - n_{ij}^{(k)} + t_{kij}^* + r$  and  $\tilde{d}_{kij}^{(r)} = b + (n_k + 1)M - (n_k + 1 - n_{ij}^{(k)} + t_{kij}^* + r) + 1$ . Thus, cluster-specific one-step-ahead edge prediction probability is a linear combination of two incomplete beta functions whose parameters reflect edge presence and edge absence, respectively. In turn, the expression of the coefficient  $\tilde{w}_{kr}$  in (17) can be retrieved by (13) with minor modifications: it suffices to replace  $D_k^*$  with  $T_{kij}^*$ ,  $d_k^*$  with  $t_{kij}^*$ ,  $m_{kh}$  with  $q_{khi} = \#\left\{ \{u, v\} \in \mathcal{V}^2 : \{u, v\} \neq \{i, j\}, n_{uv}^{(k)} = h \right\}$  and  $M_{kh}$  with  $Q_{khi} = q_{khi} + q_{k(n_k+1-h)ij}$ . Finally, the marginal likelihood  $p(\mathcal{G}^{(\mathcal{D}_k)})$  in (17) is analytically available and results from the joint distribution of  $\mathcal{G}^{(\mathcal{D}_k)}$  and  $A_{\mathcal{G}^*[ij]}$  by marginalizing the latter. It is given by:

$$p(\mathcal{G}^{(\mathcal{D}_k)}) = \sum_{r=0}^{D_k^* - d_k^*} w_{kr}^* \frac{\mathcal{B}(1/2; a_{kr}^*, b_{kr}^*)}{\mathcal{B}(1/2; a, b)}, \quad (18)$$

with  $a_{kr}^*$  and  $b_{kr}^*$  defined in (12) and  $w_{kr}^*$  in (13). It is worth noting that the marginal prior  $p(\mathcal{G}^*) = \int \psi(\mathcal{G}^*; \vartheta) dP_0(\vartheta)$ , appearing in  $\pi_{l0}$  in (5), can be easily retrieved for generative purposes as an instance of (16) when  $n_k = 0$ , that is  $\mathcal{D}_k = \emptyset$ . In this case,  $p(\mathcal{G}^{(\emptyset)}) = 1$  and (17) boils down to the prior expectation:

$$\mathbb{E} \left[ A_{\mathcal{G}^*[ij]} \right] = \frac{\mathcal{B}(1/2; a + 1 + A_{\mathcal{G}_0[ij]}, b + 1 - A_{\mathcal{G}_0[ij]}) + \mathcal{B}(1/2; a + 1 - A_{\mathcal{G}_0[ij]}, b + 1 + A_{\mathcal{G}_0[ij]})}{\mathcal{B}(1/2; a, b)}$$

Figure 9 shows how the cluster-specific one-step-ahead posterior predictive probability in (17) varies based on how frequently the edge between node  $\{i, j\}$  appears in the graphs belonging to the  $k$ -th cluster and the prior graph  $\mathcal{G}_0$ , with  $\tilde{p}_{kij} = 1/2$  for  $n_{ij}^{(k)} = (n_k + 1)/2$ . Moreover, as highlighted by the mixed color of each line,  $\tilde{p}_{kij}$  is symmetric with respect to the (equal) frequency of all the other edges  $\{u, v\} \neq \{i, j\}$ , meaning that the values  $n_{uv}^{(k)} = z$  and  $n_{uv}^{(k)} = n_k + 1 - z$  share the same curve. In addition, it is worth noting how  $\tilde{p}_{kij}$  is an odd function with center shifted at  $((n_k + 1)/2, 1/2)$ , meaning that  $f(x) = 1 - f(n_k + 1 - x)$  for  $\tilde{p}_{kij}$  function of  $n_{ij}^{(k)}$ . While in Figure 9 we aim at isolating the effect of differences among the  $n_{uv}^{(k)}$ 's on  $\tilde{p}_{kij}$ , Figure 10, shows, instead, the shape of  $\tilde{p}_{kij}$  for  $z = \sum_{\{u,v\} \neq \{i,j\}} n_{uv}^{(k)}$  varying in  $\{0, 1, \dots, (n_k + 1)(M - 1)\}$ , where  $n_{uv}^{(k)}$  can change across  $\{u, v\}$ . In this more realistic case, symmetries can only happen based on the value of  $q_{khi}$ . Finally, as function of  $n_{ij}^{(k)}$ ,  $\tilde{p}_{kij}$  is bounded from below and above by  $\xi_N(z)$  and  $\Xi_N(z) = 1 - \xi_N(z)$ , respectively, with  $\xi_N(z)$  being an increasing function of  $z$ . As  $N$  increases,  $\tilde{p}_{kij}$  approaches  $\xi_N(z)$  for  $n_{ij}^{(k)} < (n_k + 1)/2$

and  $\Xi_N(z)$  for  $n_{ij}^{(k)} > (n_k + 1)/2$ .

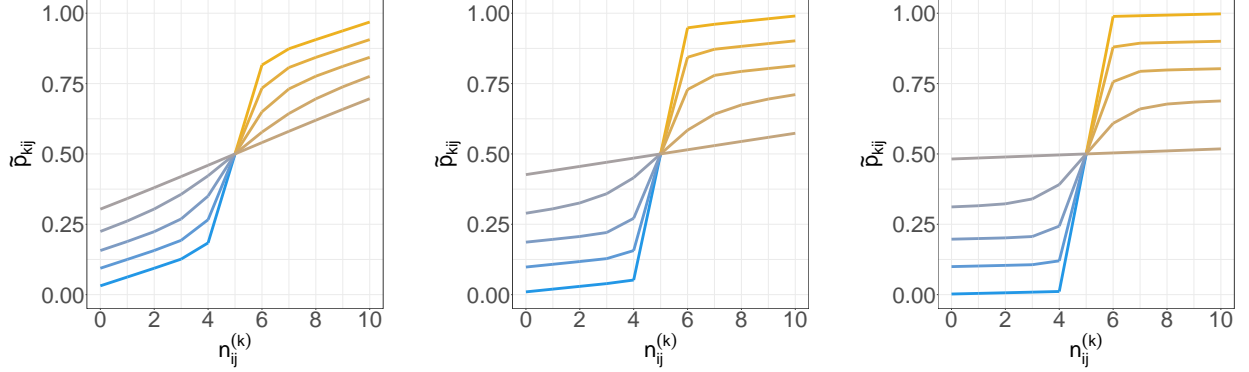


Figure 9: Probability  $\tilde{p}_{kij}$  in (17), with  $n_{uv}^{(k)} = z \forall \{u, v\} \neq \{i, j\}$ , with  $z \in \{0, 1, \dots, n_k + 1\}$  (blue for low and yellow for high) and for  $n_{ij}^{(k)} \in \{0, 1, \dots, n_k + 1\}$ , with  $n_k + 1 = 10$ , and for  $N \in \{3, 5, 10\}$  (from left to right).

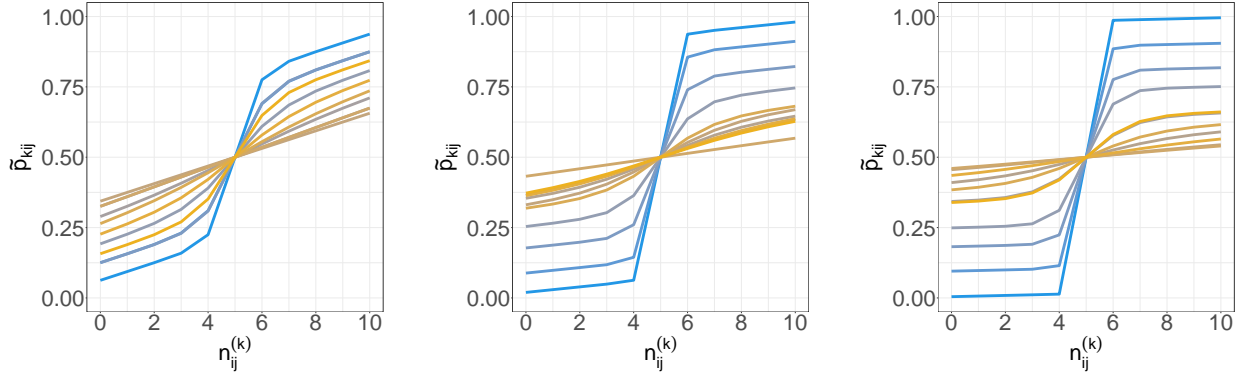


Figure 10: Probability  $\tilde{p}_{kij}$  in (17), with  $\sum_{\{u,v\} \neq \{i,j\}} n_{uv}^{(k)} = z$ , with  $z$  taking 11 equally-spaced values in  $\{0, 1, \dots, (n_k + 1)(M - 1)\}$  (blue for low and yellow for high) and for  $n_{ij}^{(k)} \in \{0, 1, \dots, n_k + 1\}$ , with  $n_k + 1 = 10$ , and for  $N \in \{3, 5, 10\}$  (from left to right).

### C.2.1 CLUSTER-SPECIFIC $m$ -STEP-AHEAD POSTERIOR PREDICTIVE DISTRIBUTION

The distribution given in (16)–(18) can be generalized to make predictions on, say,  $m$  graphs jointly, conditioned to the estimated partition and on the fact that they belong to the same cluster, e.g.  $k$ -th one. Such distribution, denoted by  $p(\mathcal{G}_1^*, \dots, \mathcal{G}_m^* \mid \mathcal{G}^{(\mathcal{D}_k)})$ , is defined on the  $m$ -dimensional cartesian product  $\mathcal{G}_Y \times \dots \times \mathcal{G}_Y$  and it turns out that we can make edge-specific predictions independently, conditionally on  $\mathcal{G}^{(\mathcal{D}_k)}$ . It is thus sufficient to study the conditional distribution of  $\mathcal{H}_{[ij]}^{(1:m)} = \sum_{l=1}^m A_{\mathcal{G}_l^* [ij]}$ , given  $\mathcal{G}^{(\mathcal{D}_k)}$ , for which we get

$$\mathcal{H}_{[ij]}^{(1:m)} \mid \mathcal{G}^{(\mathcal{D}_k)} \stackrel{\text{ind}}{\sim} \text{Cat}(\tilde{p}_{kij0}, \tilde{p}_{kij1}, \tilde{p}_{kij2}, \dots, \tilde{p}_{kijm}), \quad i < j$$



where, for  $h = 0, \dots, m$ ,

$$\tilde{p}_{kijh} = \mathbb{P} \left( \mathcal{H}_{[ij]}^{(1:m)} = h \mid \mathcal{G}^{(\mathcal{D}_k)} \right) = \frac{\binom{m}{h}}{p(\mathcal{G}^{(\mathcal{D}_k)})} \sum_{r=0}^{T_{kij}^* - t_{kij}^*} \tilde{w}_{kr} \frac{\left[ \mathcal{B}(1/2; \tilde{a}_{kijh}^{(r)}, \tilde{b}_{kijh}^{(r)}) + \mathcal{B}(1/2; \tilde{c}_{kijh}^{(r)}, \tilde{d}_{kijh}^{(r)}) \right]}{\mathcal{B}(1/2; a, b)} \quad (19)$$

where  $\tilde{a}_{kijh}^{(r)} = a + n_{ij}^{(k)} + t_{kij}^* + r + h$ ,  $\tilde{b}_{kijh}^{(r)} = b + (n_k + 1)M - (n_{ij}^{(k)} + t_{kij}^* + r) + m - h$ ,  $\tilde{c}_{kijh}^{(r)} = a + n_k + 1 - n_{ij}^{(k)} + t_{kij}^* + r + m - h$  and  $\tilde{d}_{kijh}^{(r)} = b + (n_k + 1)M - (n_k + 1 - n_{ij}^{(k)} + t_{kij}^* + r) + h$ , with  $t_{kij}^*$ ,  $T_{kij}^*$ ,  $\tilde{w}_{kr}$  and  $p(\mathcal{G}^{(\mathcal{D}_k)})$  defined in Section C.2. Figure 11 shows the shape of  $\tilde{p}_{kijh}$  as function of  $h$ , varying  $n_{ij}^{(k)}$  and  $n_{uv}^{(k)}$ .

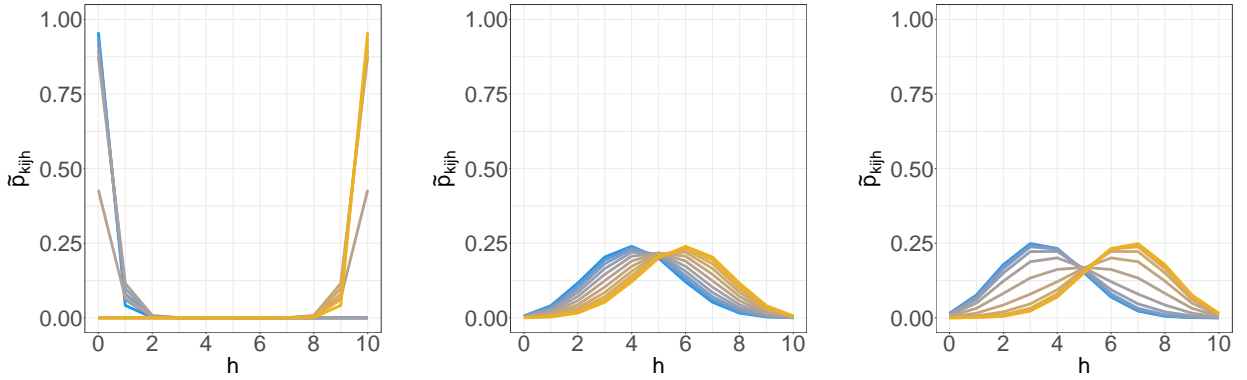


Figure 11: Probability  $\tilde{p}_{kijh}$  in (19), for  $h \in \{0, \dots, m\}$ , with  $m = 10$ , and  $n_{ij}^{(k)} \in \{0, 1, \dots, n_k + 1\}$ , with  $n_k + 1 = 10$  (blue for low and yellow for high), with  $N = 10$ , and  $\sum_{\{u,v\} \neq \{i,j\}} n_{uv}^{(k)} = z$ , with  $z \in \{0, (\frac{n_k+1}{2})(M-1), (n_k+1)(M-1)\}$  (from left to right).

### C.3 CLUSTER-SPECIFIC POSTERIOR DISTRIBUTION OF $\mathcal{G}_k^{m*}$

For each  $k = 1, \dots, \hat{K}$ , the conditional distribution of  $\mathcal{G}_k^{m*}$  given  $\alpha_k^*$  and  $\mathcal{G}^{(\mathcal{D}_k)}$  is given in (10) and (11). Here we study the conditional distribution of  $\mathcal{G}_k^{m*}$  given  $\mathcal{G}^{(\mathcal{D}_k)}$ , that we obtain from the latter by marginalizing with respect to  $\alpha_k^*$ . It turns out that:

$$A_{\mathcal{G}_k^{m*}[ij]} \mid \mathcal{G}^{(\mathcal{D}_k)} \stackrel{\text{ind}}{\sim} \text{Bern}(p_{kij}^m), \quad i < j \quad (20)$$

where the Bernoulli parameters in (20) are given by:

$$p_{kij}^m = \mathbb{E} \left[ A_{\mathcal{G}_k^{m*}[ij]} \mid \mathcal{G}^{(\mathcal{D}_k)} \right] = \frac{1}{p(\mathcal{G}^{(\mathcal{D}_k)})} \sum_{r=0}^{T_{kij}^* - t_{kij}^*} \tilde{w}_{kr} \frac{\mathcal{B}(1/2; a_{kr}^m, b_{kr}^m)}{\mathcal{B}(1/2; a, b)} \quad (21)$$

and  $a_{kr}^m = a + n_k + 1 - n_{ij}^{(k)} + t_{kij}^* + r$ ,  $b_{kr}^m = b + (n_k + 1)(M - 1) + n_{ij}^{(k)} - t_{kij}^* - r$ , with  $t_{kij}^*$ ,  $T_{kij}^*$  and  $\tilde{w}_{kr}$  defined in Section C.2, and  $p(\mathcal{G}^{(\mathcal{D}_k)})$  is given in (18).

Figure 12 shows the shape of  $p_{kij}^m$  for  $z = \sum_{\{u,v\} \neq \{i,j\}} n_{uv}^{(k)}$  varying in  $\{0, 1, \dots, (n_k + 1)(M - 1)\}$ , where  $n_{uv}^{(k)}$  can change across  $\{u, v\}$  and can serve as comparison to the probability in Figure 10.

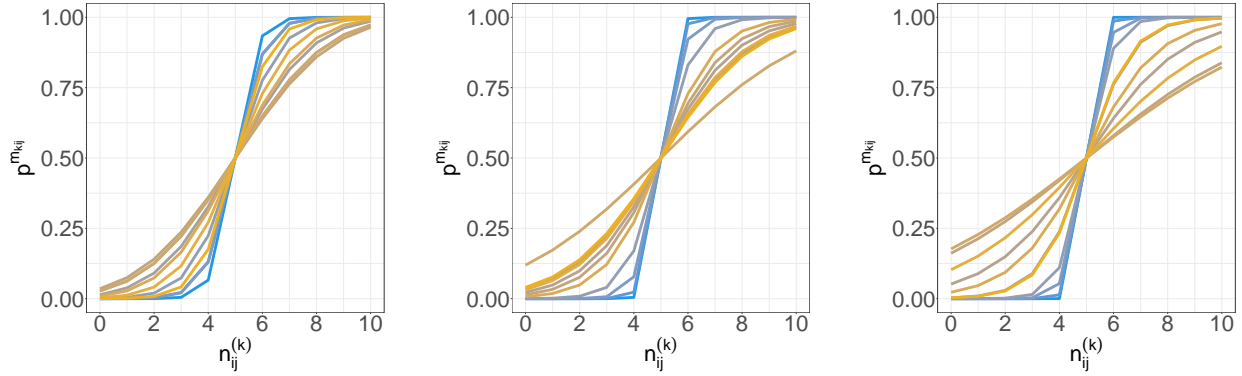


Figure 12: Probability  $p_{kij}^m$  in (21), with  $\sum_{\{u,v\} \neq \{i,j\}} n_{uv}^{(k)} = z$ , with  $z$  taking 11 equally-spaced values in  $\{0, 1, \dots, (n_k + 1)(M - 1)\}$  (blue for low and yellow for high) and for  $n_{ij}^{(k)} \in \{0, 1, \dots, n_k + 1\}$ , with  $n_k + 1 = 10$ , and for  $N \in \{3, 5, 10\}$  (from left to right).

## D FURTHER DETAILS ON THE SIMULATION STUDY OF SECTION 4

We report the specification of the parameters for the four data-generating processes used in Section 4 to generate the centroids  $\mathcal{G}_{0k}^m$ .

Graphical structure	Specification
Scale-free	We set the power law exponent of the degree distribution to 2 and the sparsity to 0.2.
Small-world	We set the degree of the lattice to 10 and the probability of rewiring to 0.2.
Stochastic Block Model	We set the number of blocks to 2, with membership probabilities equal to 1/2; the inclusion probabilities were set as 0.9 and 0.1 for diagonal and nondiagonal blocks, respectively.
Erdős–Rényi	Probability of inclusion was set to 0.3.

Table 4: Graphical structures and the corresponding parameter specification used to define the distribution centroids.

### D.1 VARYING SAMPLE SIZE WITH $\mathbb{L}^1$ DISTANCE

We present additional simulation experiments to obtain a better understanding of how the posterior mean

$$\hat{f}(\cdot) = \mathbb{E}[\tilde{f}(\cdot) \mid \mathcal{G}^{(1:n)}] = \frac{1}{c+n} \int_{\Theta} \psi(\cdot; \vartheta) dP_0(\vartheta) + \frac{1}{T} \sum_{t=1}^T \sum_{k=1}^{K^{(t)}} \frac{n_k^{(t)}}{c+n} \psi(\cdot; \vartheta_k^{*(t)})$$

concentrates around its true value  $p_*(\cdot) = \sum_{k=1}^4 0.25 p_{\text{CER}}(\cdot; \mathcal{G}_{0k}^m, \alpha_{0k})$ , as a function of the sample size  $n$ , with  $\hat{f}$  evaluated based on the posterior sample generated from Algorithm 1. Unlike the study presented in Section 4.2, we focus here on the  $\mathbb{L}^1$  distance as a metric  $d$  on  $\mathcal{P}_{\mathcal{G}_V}$ , and study the distribution of the distance between  $p_*$  and  $\hat{f}$  for finite samples of size  $n \in \{40, 80, 120, 200\}$ . The evaluation of  $\mathbb{L}^1(p_*; \hat{f})$  requires summation over the graph space  $\mathcal{G}_V$ , which is prohibitive even for moderate  $N$ . Thus, we propose an importance-sampling approximation of  $\mathbb{L}^1(p_*; \hat{f})$ . Namely,

$$\begin{aligned} \mathbb{L}^1(p_*; \hat{f}) &= \sum_{\mathcal{G} \in \mathcal{G}_V} |p_*(\mathcal{G}) - \hat{f}(\mathcal{G})| = \sum_{\mathcal{G} \in \mathcal{G}_N} \frac{|p_*(\mathcal{G}) - \hat{f}(\mathcal{G})|}{p_*(\mathcal{G})} p_*(\mathcal{G}) = \mathbb{E}_{p_*} \left[ \frac{|p_*(\mathcal{G}) - \hat{f}(\mathcal{G})|}{p_*(\mathcal{G})} \right] \\ &\approx \frac{1}{L} \sum_{l=1}^L \frac{|p_*(\mathcal{G}) - \hat{f}(\mathcal{G})|}{p_*(\mathcal{G})}, \end{aligned}$$

with  $\mathcal{G}_l \stackrel{\text{iid}}{\sim} p_*$ , for  $l = 1, \dots, L$ . The results are presented in Figure 13, which shows that the posterior estimate  $\hat{f}$  gets closer to  $p_*$  as the sample size increases. Our model appears to converge to  $p_*$  faster than the models proposed by Durante et al. (2017) and Young et al. (2022). This additional study gives credibility to the robustness of our model with respect to the choice of the metric  $d$  on  $\mathcal{P}_{\mathcal{G}_V}$ .

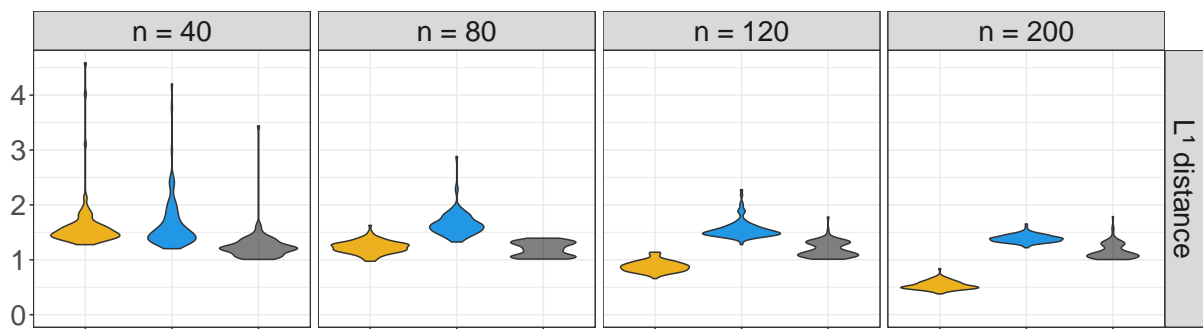


Figure 13: Importance-sampling approximate distributions of  $\mathbb{L}^1(p_*, \hat{f})$  distance for our method (yellow violins), and the methods of Durante et al. (2017) (blue violins) and Young et al. (2022) (gray violins). Distributions are estimated based on the analysis of 100 datasets.

## E FURTHER DETAILS ON ILLUSTRATIONS IN SECTION 6

We present additional plots related to the application in Section 6.

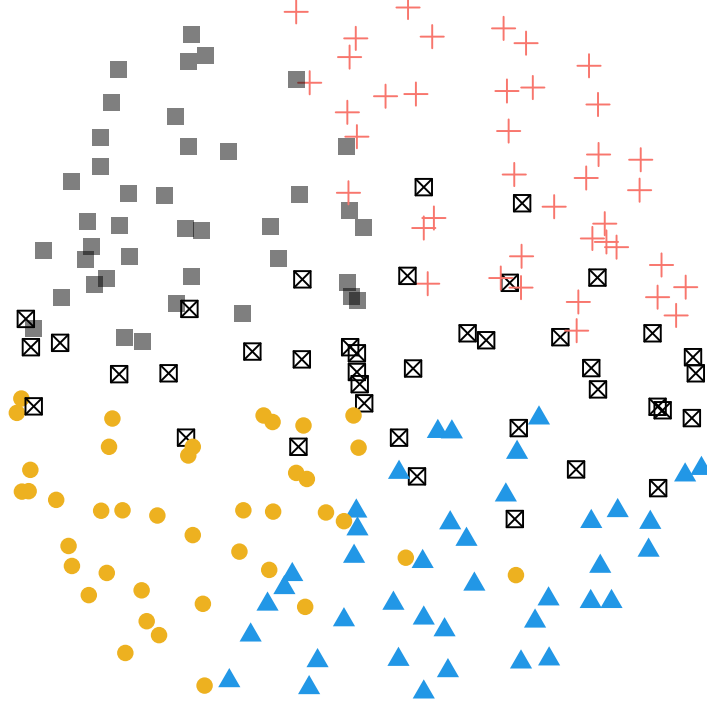


Figure 14: A 2-D visualization (top-down projection) of the atlas with 200 ROIs, where colors and shapes represent the  $m_{\text{sub}} = 5$  node cluster memberships identified through balanced clustering with  $N_{\text{sub}} = 40$ .

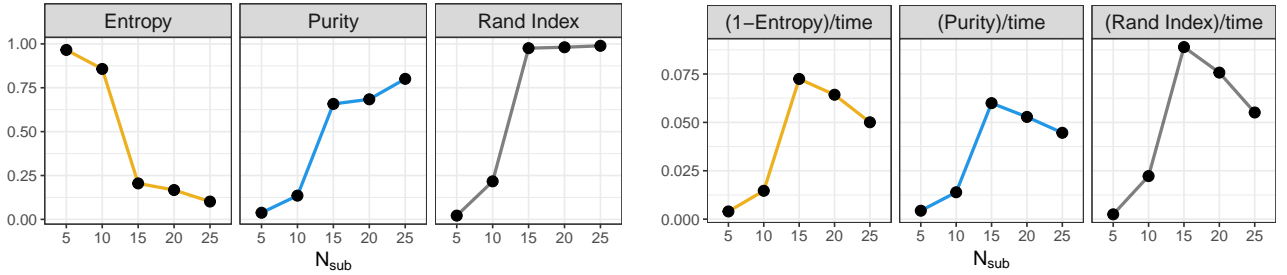


Figure 15: Clustering metrics comparing the partition estimated based on the consensus subgraph approach, with the one estimated with exact method on 48 ROIs, for the Human Brain dataset based on 48 ROIs, for  $N_{\text{sub}}$  ranging in  $\{5, 10, \dots, 25\}$ .

## E.1 CONSENSUS SUBGRAPH CLUSTERING FOR LARGE $N$ WITH NODES PARTITIONED AT RANDOM

For comparison with the analysis in Section 6, we performed consensus subgraph clustering on the human brain datasets, with 48 and 200 ROIs, by partitioning the nodes randomly, thus without utilizing the available spatial information on the nodes. This allows us to understand the impact of incorporating spatial information when partitioning the nodes. Interestingly, when nodes are partitioned at random, the clustering metrics computed on the estimated data clustering appear only slightly worse than those obtained in Section 6 based on the available spatial information. The results of our analysis are presented in Figure 16 and Table 5.  $N_{\text{sub}}$  was set equal to 15 for both versions of the human brain datasets.

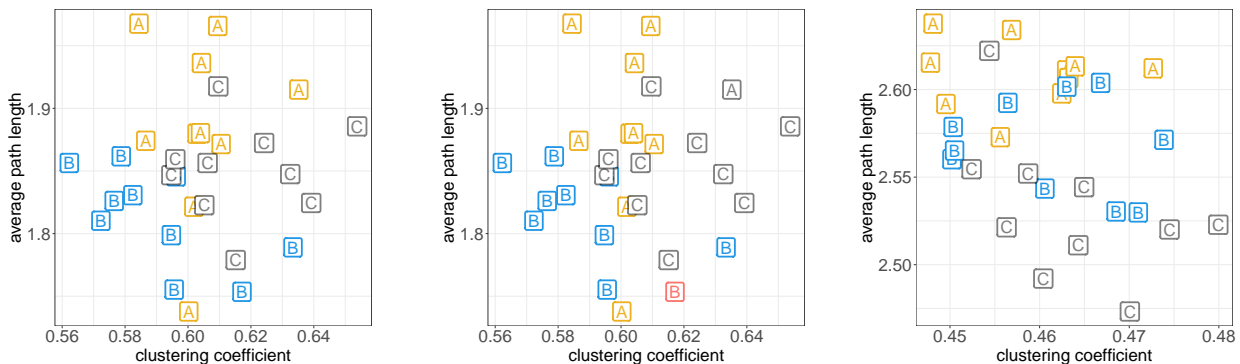


Figure 16: Scatter plots for the small-world properties of brain networks for three subjects in the dataset. Colors indicate the cluster membership, letters refer to the subject ID in the dataset, namely 0025443 (A), 0025445 (B) and 0025446 (C). Left panel:  $N = 48$ , partition estimated via DP mixture of CER kernels. Central panel:  $N = 48$ , partition estimated via consensus subgraph clustering with nodes partitioned at random. Right panel:  $N = 200$ , partition estimated via consensus subgraph clustering with nodes partitioned at random. See Figure 6 for a comparison.

$N$ ( $N_{\text{sub}}$ )	$\hat{K}$	Entropy	Purity	Rand Index
48 (15)	30	0.1420	0.7970	0.9772
200 (15)	31	0.0162	0.9699	0.9970

Table 5: Human brain dataset. Estimated number of clusters and clustering metrics comparing the partition estimated based on the consensus subgraph clustering approach, with nodes partitioned at random, with the one implied by the presence of 30 individuals in the study. See Table 3 for a comparison.

## REFERENCES

Arnqvist, N. P., V. Voinov, R. Makarov, and Y. Voinov (2022). *nilde: Nonnegative Integer Solutions of Linear Diophantine Equations with Applications*.

- Durante, D., D. B. Dunson, and J. T. Vogelstein (2017). Nonparametric bayes modeling of populations of networks. *Journal of the American Statistical Association*.
- Halberstam, H. (1967). Collected papers of g. h. hardy: Including joint papers with j. e. littlewood and others. *Journal of the London Mathematical Society s1-42(1)*, 753–755.
- Sethuraman, J. (1994). A constructive definition of dirichlet priors. *Statistica Sinica 4(2)*, 639–650.
- Voinov, V. G. and M. S. Nikulin (1997). *On a Subset Sum Algorithm and Its Probabilistic and Other Applications*, pp. 153–163. Boston, MA: Birkhäuser Boston.
- Young, J.-G., A. Kirkley, and M. E. J. Newman (2022). Clustering of heterogeneous populations of networks. *Physical Review E 105*, 014312.